Spring 2023

Numerical Modeling of Firebrand Transport

Antonio Q. Cervantes
San Jose State University

NUMERICAL MODELING OF FIREBRAND TRANSPORT

A Thesis

Presented to

The Faculty of the Department of Mechanical Engineering

San José State University

In Partial Fulfillment

of the Requirements for the Degree

Master of Science

by

Antonio Q. Cervantes

May 2023

The Designated Thesis Committee Approves the Thesis Titled

NUMERICAL MODELING OF FIREBRAND TRANSPORT

by

Antonio Q. Cervantes

APPROVED FOR THE DEPARTMENT OF MECHANICAL ENGINEERING

SAN JOSÉ STATE UNIVERSITY

May 2023

Ali Tohidi, Ph. D	Department of Mechanical Engineering
Adam Kochanski, Ph. D	Department of Meteorology and Climate Science
Farzan Kazemifar, Ph. D	Department of Mechanical Engineering

ABSTRACT

NUMERICAL MODELING OF FIREBRAND TRANSPORT

by Antonio Q. Cervantes

Firebrand showers are the fastest and most complex form of wildfire spread by generating spot fires in random locations. This randomness is due to many factors, including turbulent wind and particle shape. This work seeks to understand how small-scale turbulence affects firebrand landing distribution and develop a methodology to couple firebrand transport with wildfire simulations. Understanding transport at small scales can provide knowledge on large-scale transport in wildfire simulations. The computational domain and the mesh size in wildfire simulations are very large and do not feature small-scale turbulence. High-resolution small-scale turbulent and uniform boundary layers at various turbulence intensities are used for testing plate and rod firebrand transport. Plates and rods were found to have higher travel distances in uniform flows. Plates were also found to be more sensitive to changes in turbulence intensity. Rods were found to have a high concentration of depositions in a small area, while plates had a wide range of depositions. The shape of the firebrand was found to be an important factor in where it will land due to small-scale turbulence. The firebrand transport solver was coupled with WRF-SFIRE for large-scale transport in a high-wind-speed prescribed fire and a low-wind-speed wildfire. Both plates and rods were found to travel farther distances in the low-wind-speed fire due to higher lofting by the fire plume. This work provides the first steps toward improved wildfire simulations with firebrand transport of plates and rods. Further development can help the wildfire science community better understand wildfire spread through spot fire generation by firebrands.

ACKNOWLEDGEMENTS

I would like to thank Dr. Ali Tohidi, Dr. Adam Kochanski, and Dr. Farzan Kazemifar for all their guidance and help on this project. I'd also like to acknowledge the support from the SJSU Tower Foundation, National Science Foundation (NSF), Industry Advisory Board (IAB) members of the NSF-IUCRC Wildfire Interdisciplinary Research Center (WIRC), and most importantly, Dr. Adam Kochanski for providing sample simulation data of wildfire plumes using WRF-SFIRE. The SJSU Tower Foundation and the NSF under Grant No. 21-1505-6347 partially support this work. Any opinions, findings, conclusions, or recommendations expressed in this material are those of the author and do not necessarily reflect the views of the NSF.

TABLE OF CONTENTS

LIST OF TABLES

LIST OF FIGURES

1 INTRODUCTION

Wildfires have destructive and long-lasting effects on wildlands and urban interfaces. In 2021 there were approximately 60,000 wildfires in the United States with 7.1 million acres burned [1]. The largest fire in 2021 was the Dixie fire in California which burned over 900,000 acres and cost over 637 million dollars in damages [1]. A major contributor to the spread of wildfires is firebrand showers [2], [3]. Firebrands are pieces of burning material that are lofted by buoyant fire plumes and transported via wind [2]. Firebrands can land in random locations ahead of the main firefront which can cause spot fires [3]. This inherent randomness is due to various factors including wind turbulence, landscape topography, fuel moisture levels, and more [2], [3].

1.1 Literature Review

1.1.1 Mechanisms of Wildfire Spread and how Firebrands Contribute

The three main mechanisms of wildfire spread are radiative heat transfer, convective heat transfer [4], and spot fires due to firebrands. Spot fires are secondary fires outside of the primary fire due to the ignition of unburned dry material [5]. Evidence suggests that spot fires have a significant role in wildfire spread, especially ones in the wildland-urban interface (WUI) [2]. The generation of spot fires is a complex process due to its nonlinearity and the large number of variables including topography, wind conditions, fuel moisture, and more [3]. However, firebrand showers are a known cause of spot fire ignitions [2], [3]. Firebrands can carry high heat energy for long periods of time, and upon deposition, they can ignite fuels [3]-[6].

Firebrands are generated from drag force induced by the buoyancy of the fire plume [3]. When a firebrand breaks off, it is pushed upward into the atmosphere and then travels down-wind until it lands at a new location which potentially ignites a spot fire [2], [3]. This process is known as firebrand showers, where a large number of firebrands can rain down onto unburned

locations [3]. Firebrands have the potential to cross far distances and over many barriers such as rivers, hills, buildings, and more [6]. This makes structures such as buildings and houses, especially those in the wildland-urban interface (WUI), very vulnerable to wildfires [2], [5], [6]. Many studies have shown that firebrand showers ignite and spread WUI fires through deposition on structures [2] and wildfires through deposition on unburned fuel [3].

1.1.2 Firebrand Transport Process

The process of fire spotting via firebrands involves generation, lofting, transport, and deposition [3]. There have been investigations into these phenomena where modeling and experimentation have good agreement [3]. The process of firebrand generation was studied in a Ph.D. thesis by Tohidi et al. [3] where a mechanical break-off model is shown to represent these dynamics. The model assumed that the firebrands were cylindrical in shape, which was similar to the experimental data of Mell et al. [7] and Koo et al. [8]. This model informed that the upward drag forces by a fire plume cause shear forces and bending moments on the branches of a tree that break off firebrands [3]. The break-off mechanical model from Tohidi closely matched experimental data which led to the ability to generate virtual firebrands for simulations [3]. The data from Tohidi's thesis showed that there is a correlation between firebrand trajectory and vertical lofting caused by the upward drag force from the fire plume.

Firebrand lofting is also carried out by the buoyancy of the fire plume. This carries the particles upwards into the atmospheric boundary layer [3], [4]. The formation of bent-over smoke plumes, which are pushed in the direction of the wind, is known to spread firebrand showers [3]. The cross section of most fire plumes has been observed to form in the shape of an ellipse where its vertex points in the direction of wind [3], [9], [10]. This means that the trajectory of firebrands is likely to be in the direction of the wind. However, turbulence has been observed to alter the trajectory of firebrands. A paper by Tohidi et. al. [11] showed that spherical firebrands had shorter predicted travel distances in turbulent flows than in uniform

flows.

The phenomena in which firebrands follow the direction of the wind can be seen in a turbulent transport model developed by Mankame et al. [6], where firebrands are released over variously sized blocks. In these simulations, the effects of turbulence revealed that the rear side of the block, where flow separation occurs, had no firebrands deposited onto it [6]. This effect is due to the acceleration of wind flow on the front side (leading edge) and top panels of the block. This placed extra momentum on the firebrands and caused them to not deposit on the rear side (trailing edge) and flow downstream with the wind [6]. Wind flow direction and velocity have a major influence on the trajectory of firebrands.

1.1.3 Modeling of Particle Transport

Past studies on modeling firebrand transport have used debris transport equations to represent the dynamics of firebrand flight [3], [6]. Studies have shown that the geometric shape of firebrands can alter the trajectory of their flight [3], [12]. For example, disc-shaped firebrands can travel further than spherical shapes [12], [13]. Non-spherical firebrands have rotational effects that differ from spherical shapes [3]. Studies on this phenomenon were conducted by Richards et al. [14], [15], who found that the geometry of the particles, the angle of attack and the angle of tilt with respect to the airstream alter the drag and moment coefficients on the particle. Studies by Sardoy et al. [6] have shown that these differences in geometric shapes cause non-spherical shapes to have travel distances longer than spherical ones.

Debris transport has many uncertainties due to turbulent wind [16]. A thesis, written by Grayson et al. [17], addressed these issues by applying a statistical distribution to the dynamics equations for debris trajectories. This probabilistic model matched experimental wind-tunnel test data and proved an applicable method for predicting debris trajectories [17]. It can be seen that geometric shape is an important aspect of firebrand trajectory because of its varying aerodynamics [16], [17], and rotational effects [3].

1.2 Objectives

Turbulent flows contain eddies of multiple length scales [18]. While modern computational fluid dynamics (CFD) codes are capable of simulating a wide range of turbulence scales **Bartholomew2020**, wildfire simulations have difficulties in modeling small scales due to their large domain and mesh sizes [19]. Computational simulations are still an essential tool to wildfire research because real-world experiments of firebrands are difficult to conduct due to their complexity and variability [2]. This reveals a gap in knowledge on the influence of small-scale turbulence on firebrand landing location. Questions on how turbulence influences firebrand transport are:

- How sensitive are firebrands to change in turbulence intensity?
- How does firebrand landing distribution differ with varying geometric shapes?

Answering these questions can help understand where firebrands will land in turbulent flows. Understanding turbulence can increase the accuracy of wildfire prediction models by implementing spot fire generation from simulated firebrands. This is vital for understanding how wildfires spread by spot fires, which could improve wildfire threat management and suppression.

2 METHODOLOGY

A high-resolution LES model is used to simulate small-scale turbulent boundary layers with a mesh size of 2.5 cm at 4% and 7% turbulence intensity. The data from the CFD code is coupled with a firebrand transport solver for the simulation of plate and rod particle transport in small-scale turbulence. The firebrand transport solver is then coupled with WRF-SFIRE to simulate transport in large-scale wildfire domains with mesh sizes 250-300 m and varying topography and wind conditions. The landing distributions and travel distances are analyzed using statistical methods.

2.1 CFD Coupling

The firebrand transport code uses a one-way coupling method with CFD data by reading the velocity field and time from the solver outputs as a 4-dimensional dataset. The firebrand transport code uses the CFD flow time as the global timeline and calculates particle trajectories at small consecutive time steps. Particles are initialized at the beginning of the global time, and when all the particles land the simulation ends.

2.2 WRF-SFIRE Coupling

The firebrand transport model uses a two-way coupling method with WRF-SFIRE to simulate spot fire generation through firebrands shaped as plates and rods. Integration of non-spherical firebrand shapes was crucial for assessing transport physics on a large scale. Analysis of these physics can provide insight into the mechanisms of spot fire phenomena. The coupling process starts with the firebrand transport code reading the WRF-SIRE output and restart files. Wind velocity, topography, and fire flux location data are read from the output files. Then, firebrands are initialized in the locations of the active fire where the fire flux is greater than 1. This allows the firebrands to be lofted vertically from the buoyancy of the fire plume. The height

of initialized particles is based on the elevation of the topography. The number of initialized firebrands is a user-defined variable and is arbitrarily set to 100 particles for this study. Next, the firebrand trajectories are calculated, and their depositions are recorded. The depositions are added to the ignition time variable of the restart file and then sent back to WRF-SFIRE. Figure 1 shows a flow chart of the coupling process.

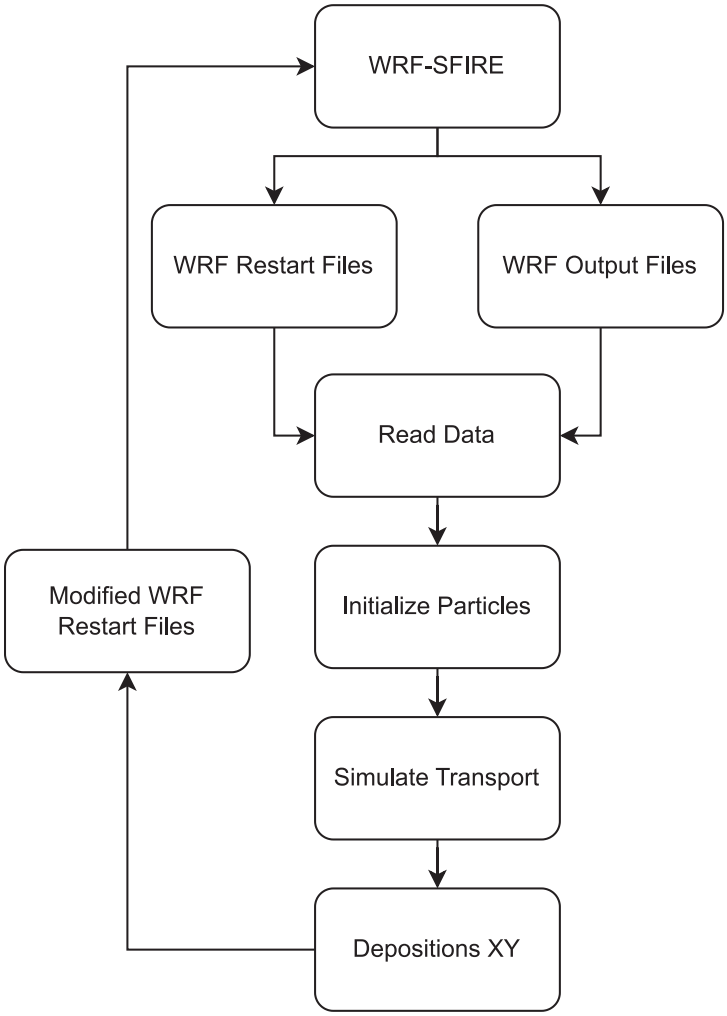

Fig. 1. Flowchart of WRF-SFIRE coupling process with the firebrand transport solver

The coupling method uses a staggered data sharing scheme. The process works by having WRF-SFIRE and the firebrand transport solver run simultaneously on the same global timeline with timestep Δt_G. As WRF marches through time, data is sent to the firebrand transport solver

and particles are initialized based on that data. The particles are initialized at the same timestep as the global timestep. The firebrand solver computes the trajectories at a timestep Δt_f, then adds depositions to the restart files, and sends them back to WRF-SFIRE. Particle trajectories are calculated in a timestep smaller than the global timestep ($\Delta t_f < \Delta t_G$), and before the end of the global timestep, depositions are sent forward in time to the next step of the global timeline. This process is repeated until the end of the WRF-SFIRE simulation. Figure 2 outlines the time-marching process. Firebrand depositions are gathered when a particular location reaches a user-defined threshold. The threshold value is arbitrarily set as 100 to define the number of firebrands to ignite a spot fire.

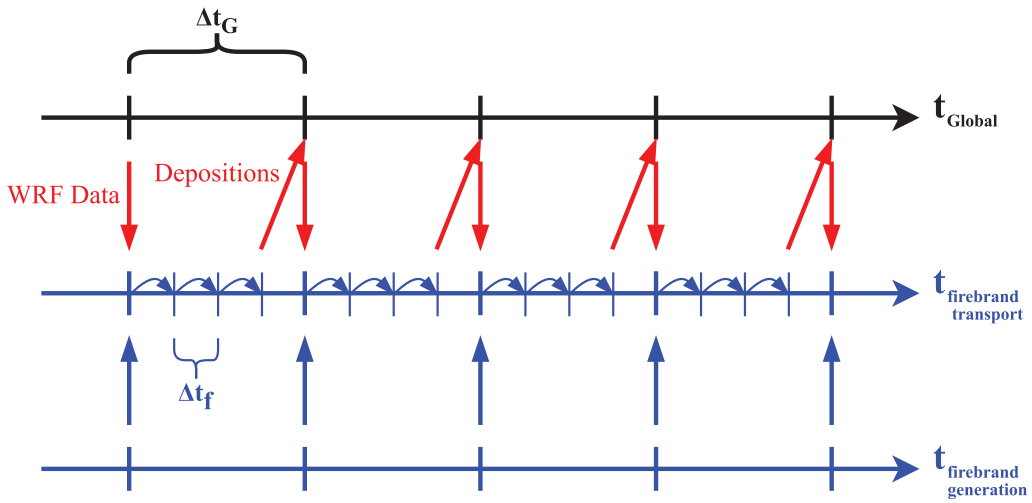

Fig. 2. Diagram of WRF-SFIRE coupling time march process with the firebrand transport solver

3 GOVERNING EQUATIONS

3.1 Geometry

The firebrand transport model used in this study simulates plate and rod particle shapes. These shapes were chosen based on experimental data of firebrand collection which showed plates and rods occurred the most from burning trees [20], [13], [21], [22]. These shapes are also non-spherical which is typically not seen in coupled firebrand-wildfire simulations due to their extra physics for rotation. The geometry of the firebrand can alter the drag forces and moments exerted on its body [14], [16]. The particle's length l_z, width l_y, and thickness l_x are its dimensions where $l_x < l_y < l_z$ [16]. Figure 3 shows a diagram of the rod and plate firebrand dimensions.

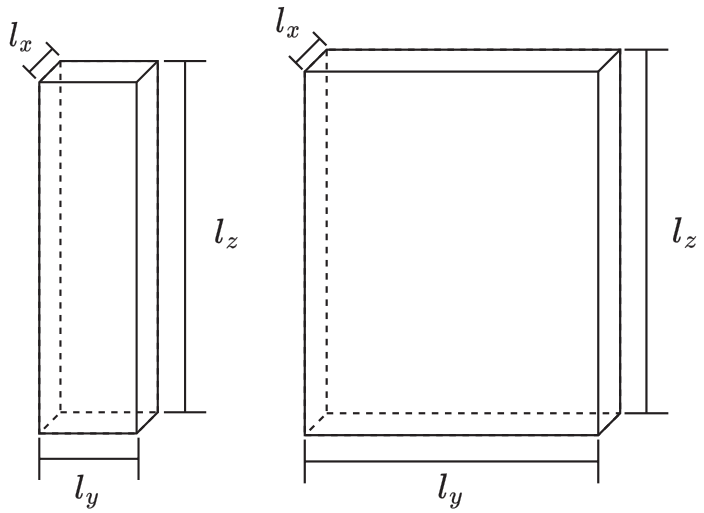

Fig. 3. Dimensions of rod (a) and plate (b) firebrands

3.2 Coordinate Systems

The coordinate system that firebrands operate on is a fixed inertial frame of reference $I(O,X,Y,Z)$. The inertial frame of origin O does not translate or rotate [23]. The position

vector ($\vec{R}_c$) and velocity vector ($\vec{V}_c$) of the firebrand particles are described by the body-fixed frame $B(c,x,y,z)$. The body-fixed frame translates and rotates with the particle's principle axis, and its origin is located at the center of mass c [23]. Figure 4 shows a diagram of the inertial frame, body-fixed frame, and position vector of a rod firebrand.

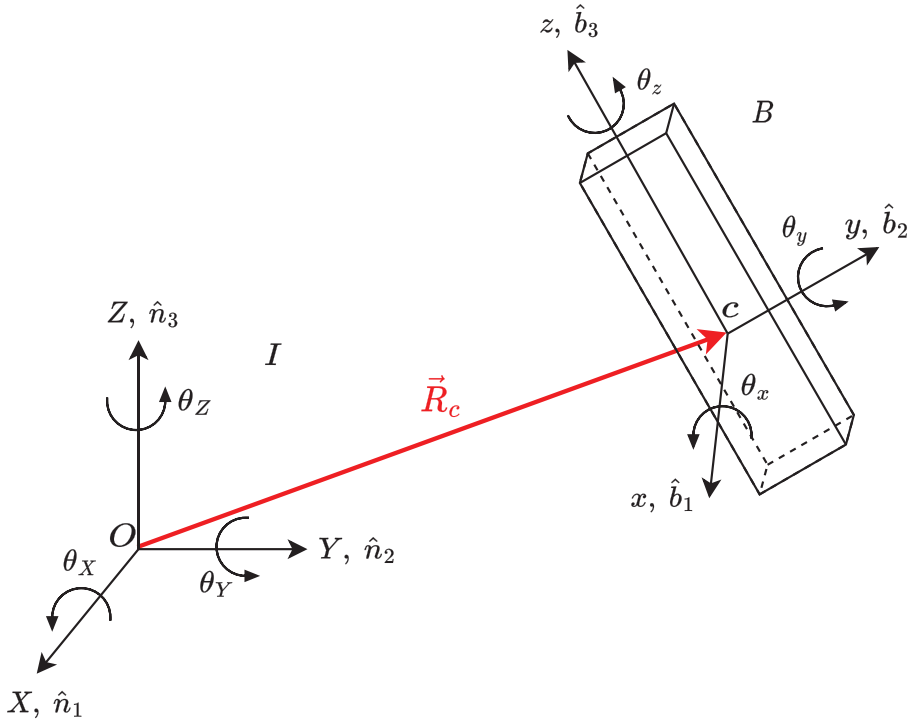

Fig. 4. Diagram of a plate-shaped particle and its body-fixed frame

3.3 Aerodynamics

The firebrand transport model solves the 6-degree-of-freedom particle dynamics equations from current literature [17], [6]. The model solves for linear and angular momentum seen in equations 1 and 2 [3].

$$\ddot{\vec{x}} = \frac{1}{m}\vec{f} - g\vec{j} \tag{1}$$

$$\vec{L_p} = \vec{M}_p - \vec{\omega} \times \vec{L_p} \tag{2}$$

Where f is the external drag forces, g is gravitational acceleration, $\vec{L_p}$ is angular momentum, $\vec{\omega}$ is rotation rate, and $\vec{M}_p$ is applied moments [3]. The drag coefficient $\vec{c_f} = c_f(\varepsilon, \gamma, G)$ and moment coefficient $\vec{c_M} = c_M(\varepsilon, \gamma, G)$ are functions of angle of attack (ε), tilt angle (γ), and aspect ratio G [3], [17], [14]. The coefficients come from experimental data by Richards et. al. [14], [15]. The firebrand solver is validated with experimental data of free-falling particles [3].

4 TURBULENT BOUNDARY LAYER SIMULATIONS

4.1 CFD Solver & Turbulence Model

The CFD solver used for the turbulent boundary layer (TBL) simulation was Xcompact3d [24]. This solver uses finite difference schemes for a spectral-like method to solve the incompressible Navier-Stokes equations to sixth-order accuracy. The governing equations for the Navier-Stokes equations are [25]:

$$\frac{\partial \mathbf{u}}{\partial t} = -\nabla p - \frac{1}{2}[\nabla(\mathbf{u}\otimes\mathbf{u}) + (\mathbf{u}\cdot\nabla)\mathbf{u}] + \nu\nabla^2\mathbf{u} + \mathbf{f} \tag{3}$$

$$\nabla\cdot\mathbf{u} = 0 \tag{4}$$

where $\mathbf{u}$ is the velocity field, p is pressure field with a constant density ($\rho = 1$), and $\mathbf{f}$ is the forcing field [25]. The CFD solver uses a finite difference scheme for the first and second derivatives of equation (3), allowing it to accurately calculate a wide range of turbulence scales without being a fully spectral-based solver [25]. Fast Fourier Transforms (FFTs) are used for solving equation (4) for incompressibility [25].

The Large Eddy Simulation (LES) turbulence model is chosen for the TBL simulation. LES works by resolving eddy length scales in the large energy-containing range and inertial subrange. Small scales, also known as subgrid-scale (SGS) are in the dissipation range and must be modeled [18], [26]. Xcompact3d uses the Smagorinksy SGS model to capture the small scales [27].

4.2 Computational Domain

The turbulent boundary layer simulations were created to test firebrand transport in turbulence intensities of 4% and 7%. The TBL simulations were set up to match the boundary layer of a wind tunnel experiment conducted by Tohidi et al. [3]. Validation of the CFD data is

critical for trust in the simulation results. The computational domain parameters are shown in Table 1.

Table 1
Computational Domain Parameters of TBL Simulation

Parameter	**Symbol**	**Value**	**Unit**
Streamwise length	l_x	5	m
Channel height	l_y	2	m
Spanwise length	l_z	3	m
Grid length x	Δx	0.025	m
Grid length y	Δy	0.025	m
Grid length z	Δz	0.025	m

4.3 Initial & Boundary Conditions

The boundary conditions of the TBL simulation can be seen in Figure 5. The inlet and outlet are periodic to ensure a fully developed turbulent flow. The side walls were periodic and the top wall was free-slip. The bottom wall was set as a no-slip condition to match the physical properties of the boundary layer in the experimental wind tunnel data from Tohidi et. al. [3]. The initial conditions of the TBL simulation can be seen in Table 2.

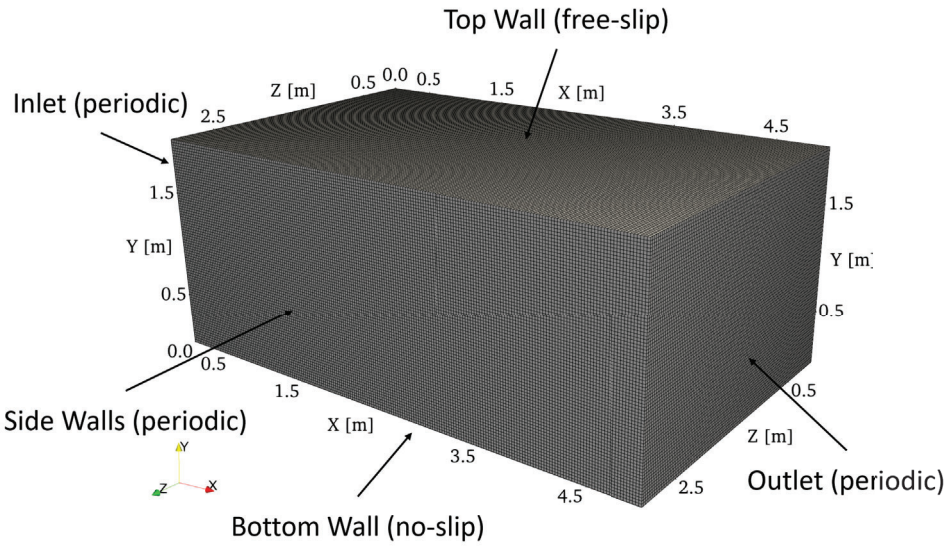

Fig. 5. Computational mesh domain of TBL simulation with boundary condition labels

Table 2
Initial Conditions of TBL Simulation

Initial Condition	**Symbol**	**Value**	**Unit**
Velocity	u_0	2.23	m/s
Reynolds Number	Re	284,000	-
Kinematic Viscosity	ν	1.568×10^{-5}	m^2/s
Reference Height	z_0	0.04	m
Power Law Exponent	α	0.16444	-

The inflow conditions were set up to match the experimental data. The power law equation was used to create the same boundary layer as the experiment results [3].

$$u(z) = u_0 \left(\frac{z}{z_0} \right)^{\alpha}$$

Where reference height z_0, reference velocity u_0, and exponent α, are the properties used to compute the boundary layer [28]. The power law exponent was taken from the experimental data. Figure 6 shows the power law velocity profile with 5% amplitude noise applied to the

initial velocity field to trigger turbulence.

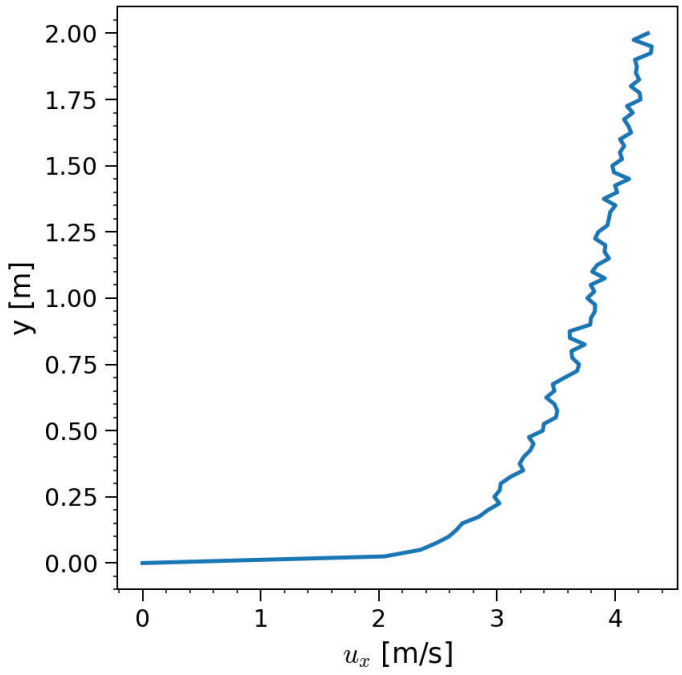

Fig. 6. Initial boundary layer of u_x velocity component with 5% amplitude noise

4.4 Validation

Turbulent boundary layer simulations were validated with the velocity profile of the experimental data of Tohidi et. al. [3]. Statistical analysis methods were used to assess the mean of the time-averaged velocity profile of the TBL simulation against the experimental data. Validation results were taken from a probe located at the center of the TBL domain (x=2.5 m, y=0-1 m, z=1.5 m). The mean boundary layer velocity profile is shown to match the experimental data in Table 3. The velocity profiles are visualized along with a power law fit line in Figure 7.

Table 3
Assesment of TBL and Experimental Results

Parameter	**Mean (I = 4%)**	**Mean (I = 7%)**
Simulation	3.13	3.07
Experimental	3.19	3.19
Percent Difference	1.77%	3.72%

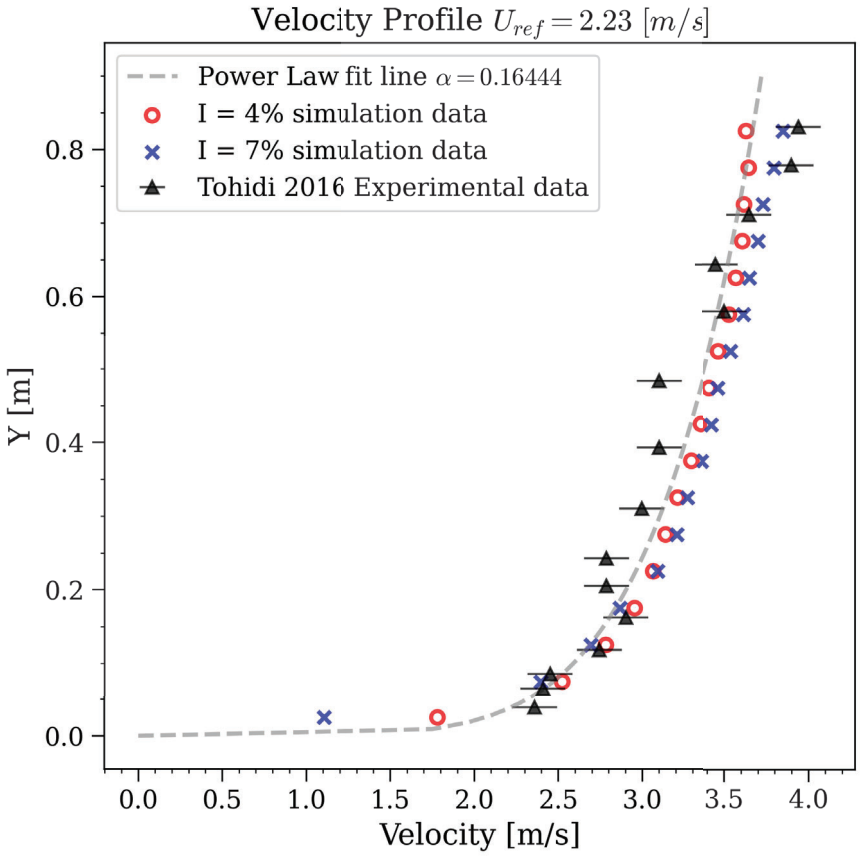

Fig. 7. Comparison of TBL simulation results for 4% and 7% turbulence intensity cases with experimental data and power law fit line.

The TBL simulations were run for 100 seconds of flow time to get a fully developed flow. It was found that from 50-100s showed a developed flow and was verified with the Kolmogorov $-5/3$ Spectrum [18]. The power spectral density (PSD) of the 4% and 7% turbulence intensity

TBL simulations are visualized in Figure 8. The slope of the u_x velocity component was estimated to match the Kologorov $-5/3$ Spectrum and confirms a fully developed flow [18], [28].

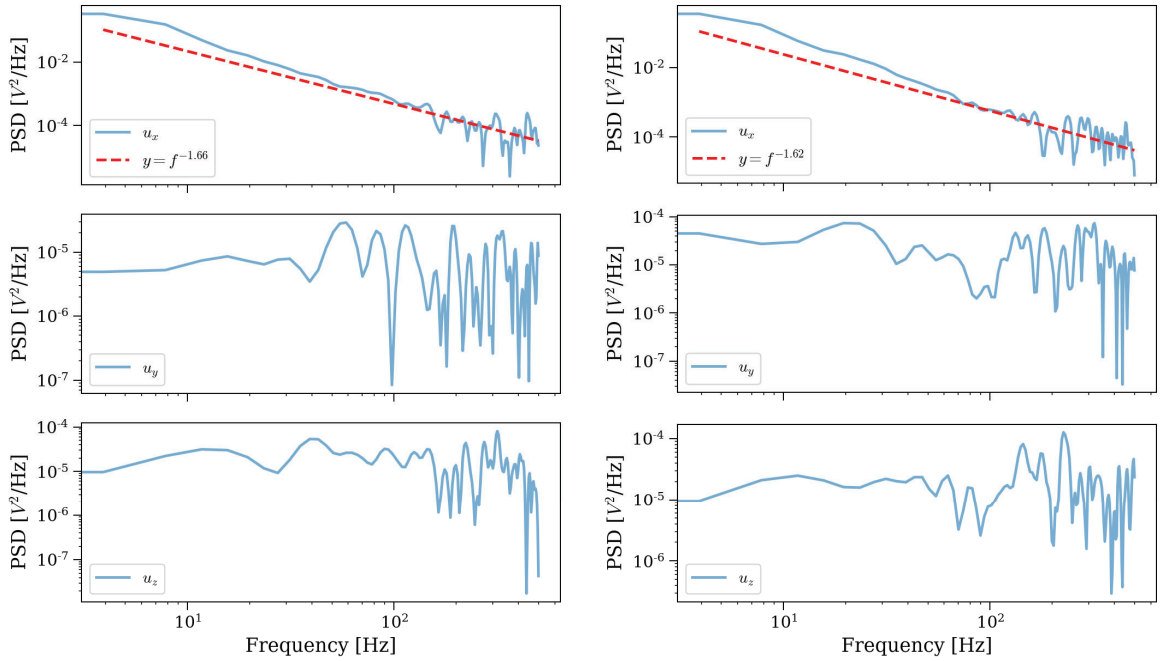

(a) (b)

Fig. 8. PSD plot of 4% (a) and 7% (b) turbulence intensity TBL simulations. The top shows the u_x velocity component and curve fit line, the middle is u_y velocity, and the bottom is u_z velocity.

4.5 Results

Results from the turbulent boundary layer simulation show very fine eddy structures in the flow. Figure 9 show the time evolution from 50 to 100 seconds of the velocity components u_x, u_y, and u_z for the 4% and 7% turbulence intensities cases. Figure 10 shows the Q-criterion of the 4% turbulence intensity case. This plot was created in Paraview and shows the q-criterion at a value of 25. The isosurfaces display the locations of vorticity in the flow, and they are colored with the velocity magnitude.

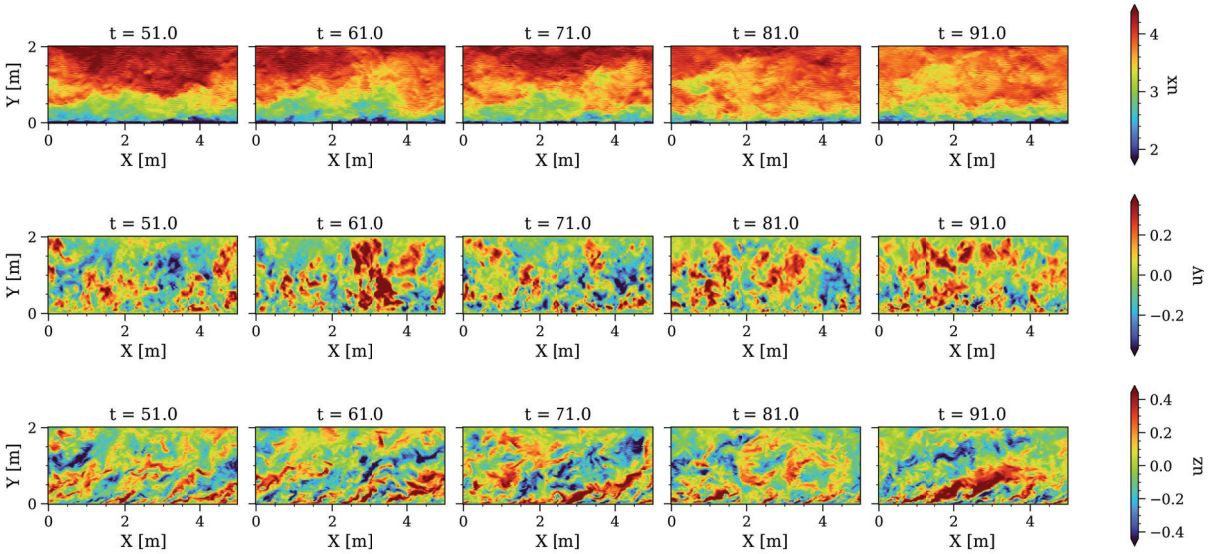

(a)

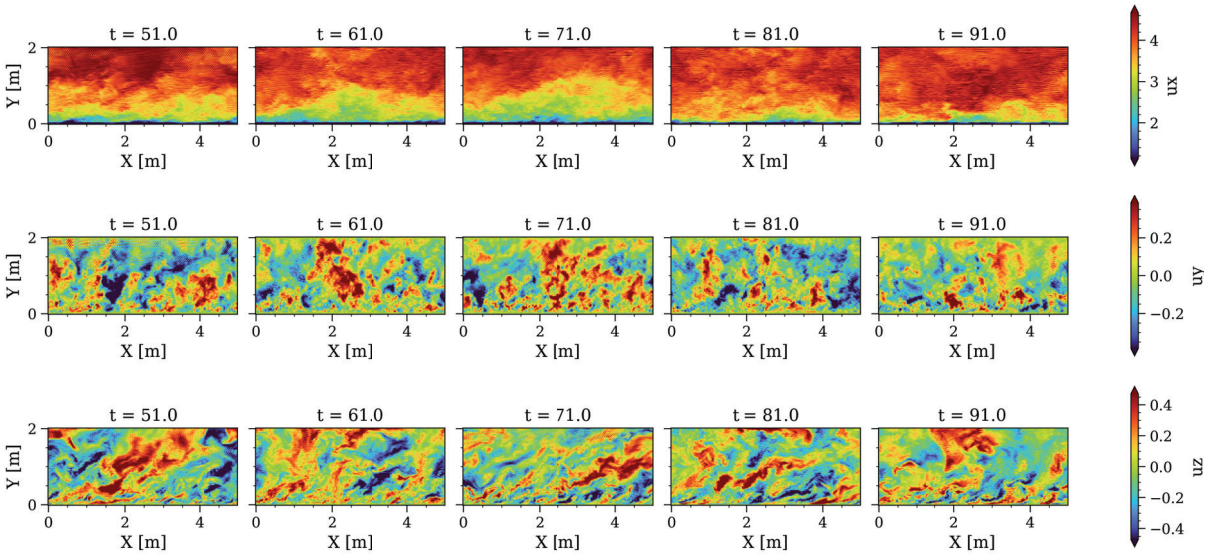

(b)

Fig. 9. Evolution of turbulent flow in the TBL simulations from 50-100s for 4% (a) and 7% (b) turbulence intensity cases. The u_x velocity component is displayed at the top, u_y in the middle, and u_z at the bottom for each turbulence intensity case.

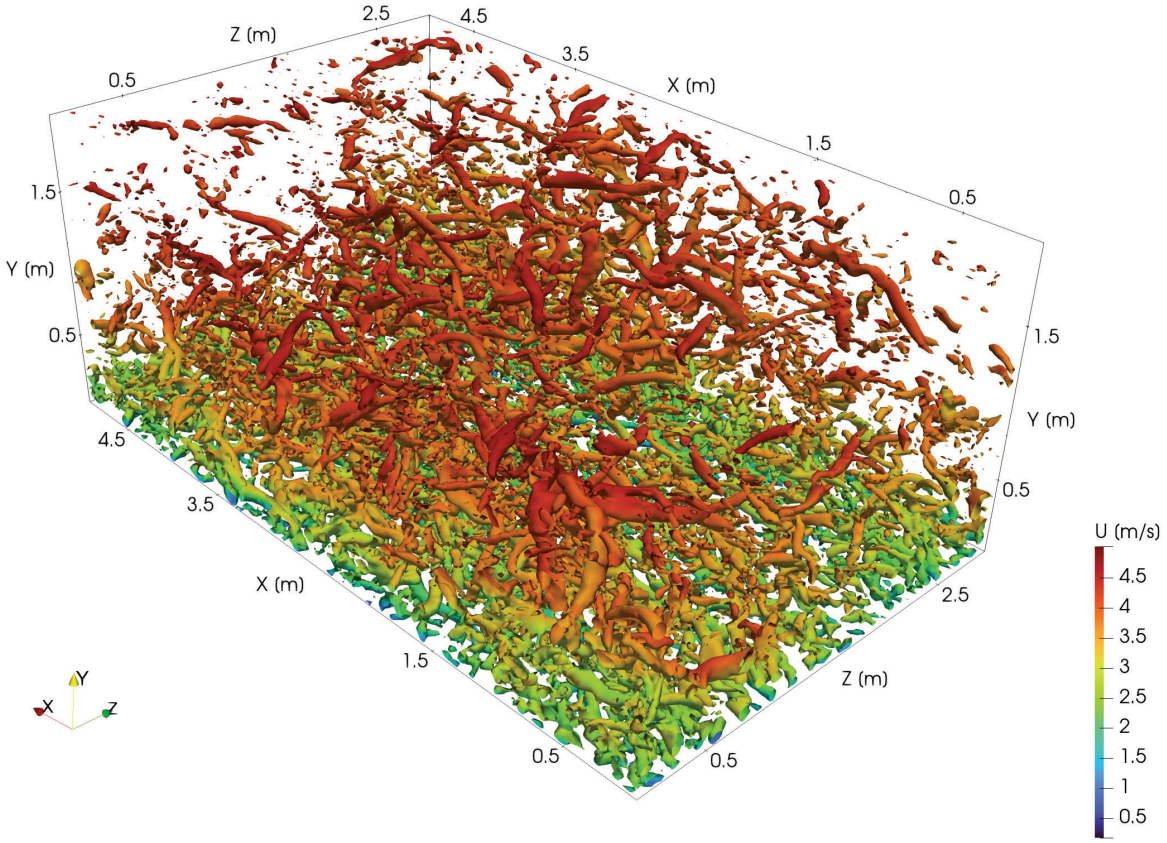

Fig. 10. Q-criterion of 4% turbulence intensity case colored by velocity magnitude

4.6 Turbulence Intensity

The 4% and 7% turbulence intensity TBL simulations were created by changing the configuration file in Xcompact3d's input parameters. The Atmospheric Boundary Layer configuration file was used for the 4% case and Sandbox configuration file was used for the 7% case. The turbulence intensity was calculated by,

$$I \equiv \frac{u'}{U}$$

where u' is the root-mean square of the instaneous velocity and U is the mean velocity [18]. The velocity data from the TBL simulations from 50-100 seconds was taken from a probe

located at x=2.5 m, y=1 m, z=1.5 m. This data was used to calculate the turbulence intensity. Figure 11 shows the fluctuations of the velocity components over time, and from these results turbulence intensities of 4% and 7% were found.

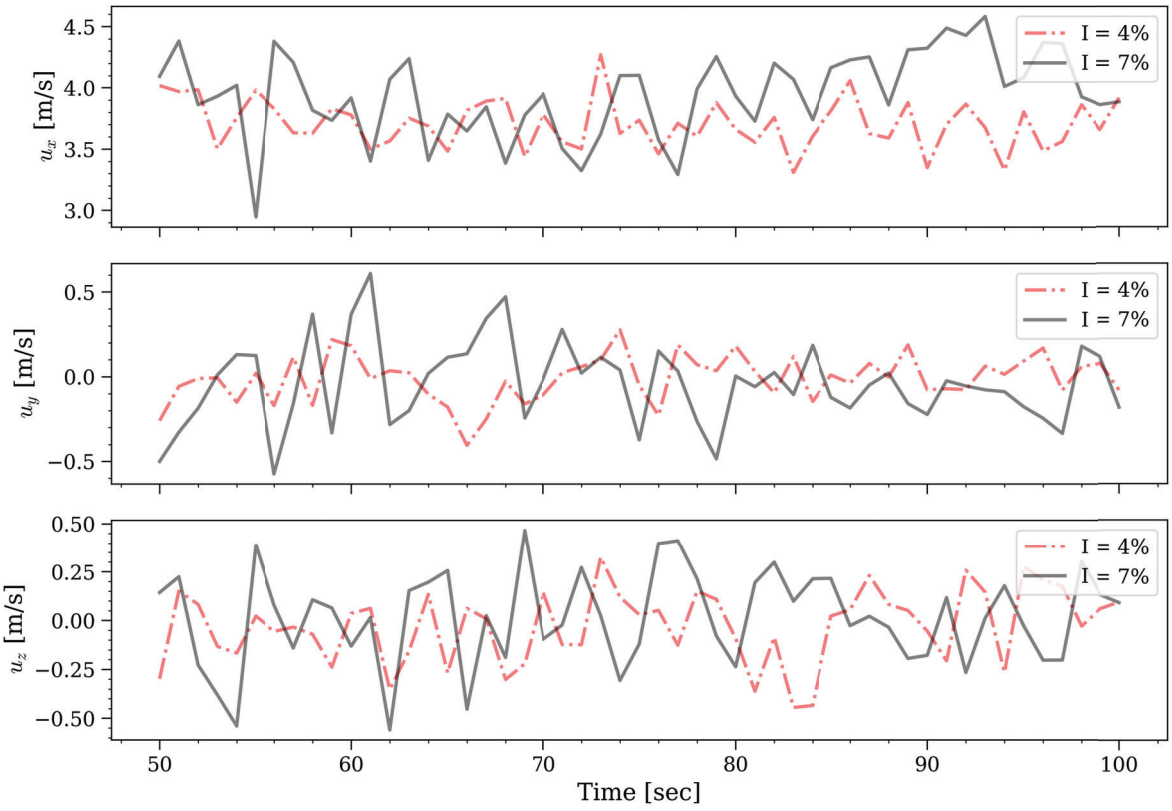

Fig. 11. TBL simulation data of u_x (top), u_y (middle), and u_z (bottom) used for turbulence intensity calculation.

5 FIREBRAND TRANSPORT

To understand how firebrand transport is affected by small-scale turbulence and how it could be related to large-scale turbulence, 36 numerical experiments were carried out for firebrand transport in both domains. Figure 12 is a simulation tree that outlines the experiments carried out to answer these questions. Firebrands were released in the velocity fields of the TBL and WRF-SFIRE simulations. The TBL simulations of 4% and 7% turbulence intensity (I) were used to understand the effects of turbulence intensity. In each of these cases, plate and rod firebrands were released to assess the influence of particle shape. For each shape, firebrands were released in instantaneous and time-average velocity fields to assess differences in turbulent and uniform flows. Finally, for each velocity field, firebrands are released at four release heights of 0.25 m, 0.75 m, 1.25 m, and 1.75 m for analysis of height and travel distance. For the WRF-SFIRE tests, there are two fire simulations. The first is Manning Creek which is a high wind speed and low-velocity fluctuation prescribed fire simulation with a Reynolds number of 5,170,572. The second is the Creek Fire simulation which is a low wind speed and high-velocity fluctuation wildfire simulation with a Reynolds number of 2,932,557. For each wildfire case, plate and rod firebrands were released at a uniform random distribution from 2-10 m height.

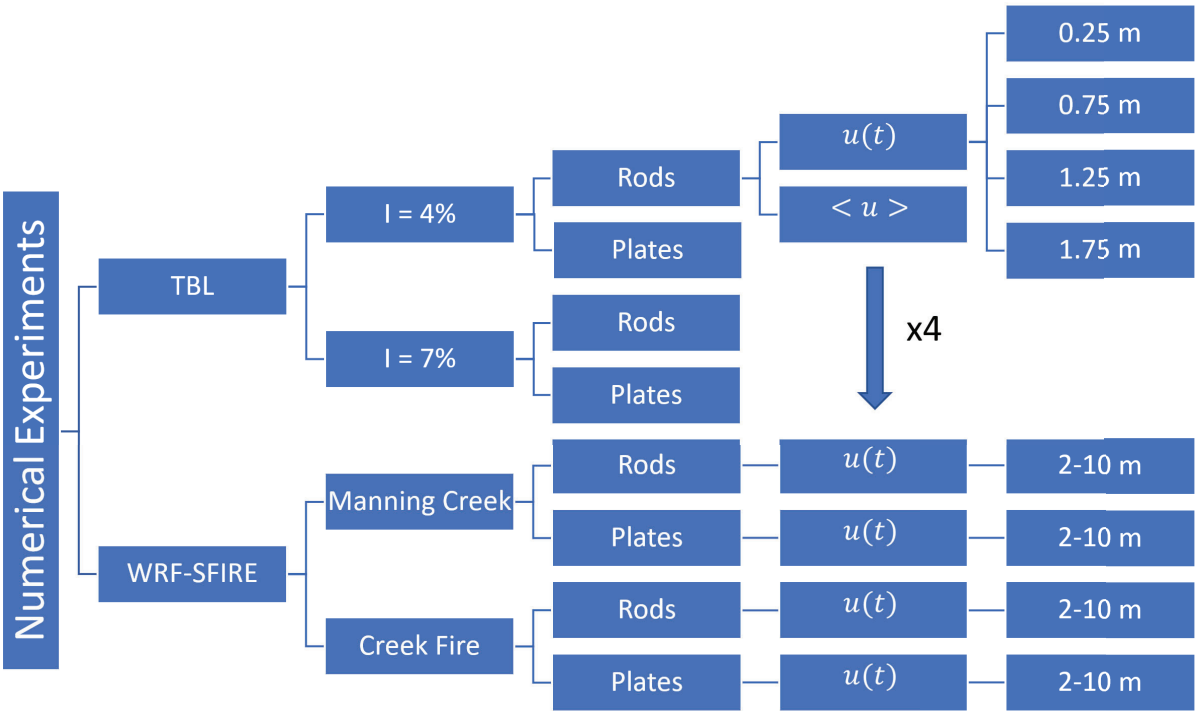

Fig. 12. Simulation tree for numerical experiments for assessment of firebrand transport in turbulent flows.

5.1 Small-scale Firebrand Transport

Experiments conducted in the small-scale firebrand transport simulations had fixed dimensions of $l_x = 3$ mm, $l_y = 15$ mm, $l_z = 25$ mm for plates, and $l_x = 3$ mm, $l_y = 5$ mm, $l_z = 25$ mm for rods. The dimensions were chosen to be near the size of experimental data of firebrands from burning trees [20], [13], [21], [22]. Each firebrand had a fixed density of 728.89 kg/m^3 to represent burning composite material from a structure. This resulted in a fixed mass of 0.82 g for plates and 0.273 g for rods. These parameters were fixed to reduce the number of random variables and complexity in the statistical analysis. A total of 1000 firebrands were released at the start of the simulation. Firebrands were released in the center of the TBL computation domain ($x = 2.5\ m,\ y = 1.5\ m$) at heights of 0.25 m, 0.75 m, 1.25 m, and 1.75 m. Each particle was oriented at a uniform random distribution from 0-2π on all 3 of its principal axes. This

was for allowing a uniform spread of depositions across all possible release orientations.

5.1.1 Results

The tumbling of the firebrands is visualized in Figure 13 which shows a three-dimensional chronograph of a plate and rod. The two particles undergo different rotation patterns based on initial orientation and the applied wind velocity. These differences lead to different trajectories between the two shapes. Figure 14 shows the trajectories of firebrands in 4% turbulence intensity at 1.75 m release height.

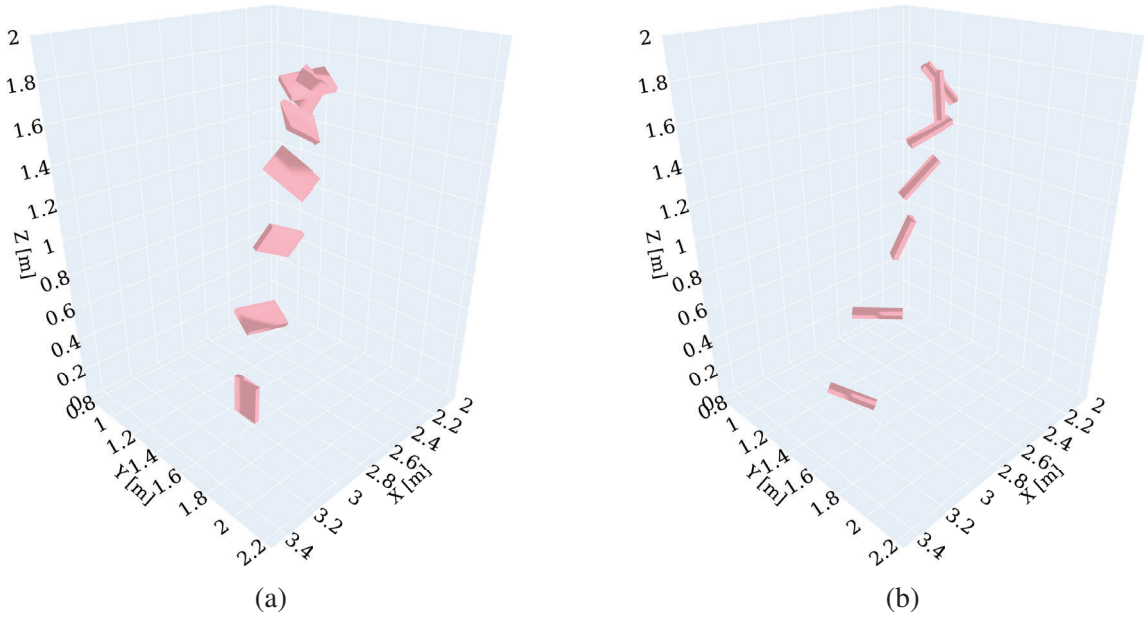

Fig. 13. Chronograph plots of 3D firebrand tumbling of a plate (a) and rod (b) particle in small-scale turbulence.

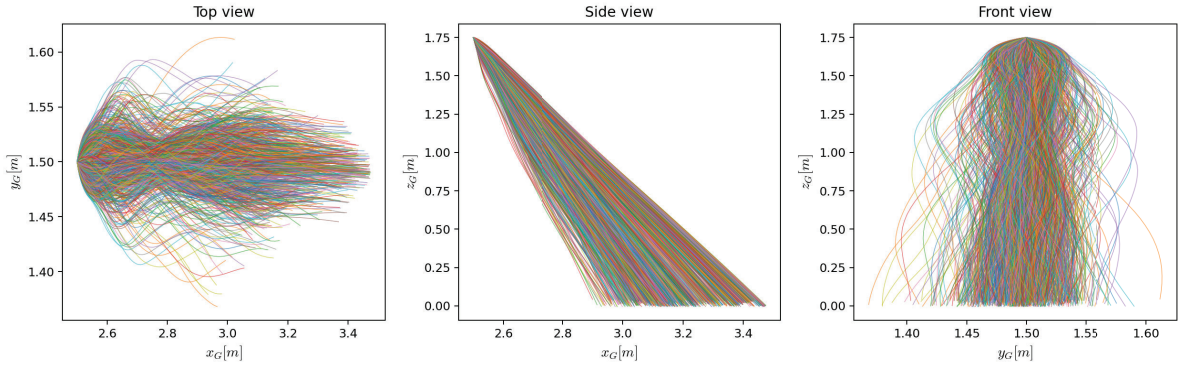

(a)

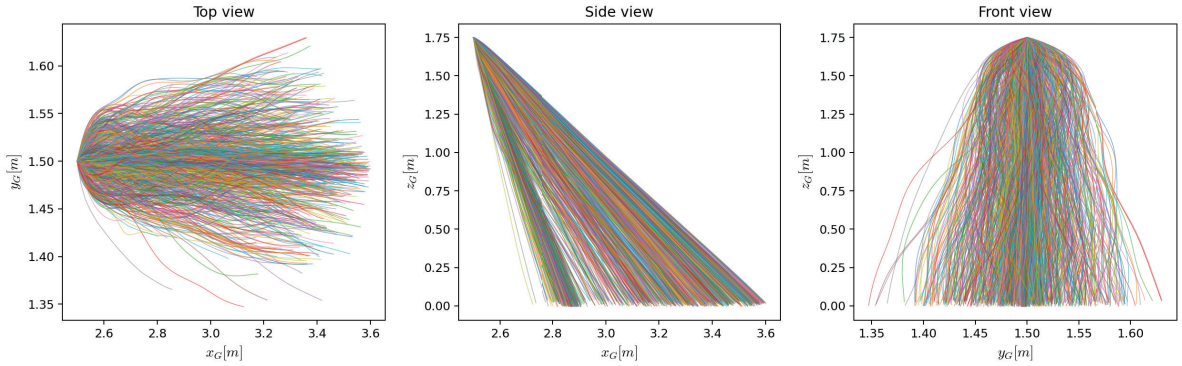

(b)

Fig. 14. Trajectories of plate (a) and rod (b) particles 4% turbulence intensity case at a release height of 1.75 m.

5.1.1.1 Particle Depositions: Results from the small-scale transport tests were analyzed for landing distribution. Statistical analysis of the landing location of the firebrand particles was performed by calculating the summation of particle deposition count over a 1x1 m^2 area. Figure 15 shows contour plots of the aggregate deposition count for plate firebrands in turbulent ($u(t)$) and uniform ($\overline{u}$) velocity fields of $I = 4\%$ and $I = 7\%$ at release heights 0.25 m, 0.75 m, 1.25 m, and 1.75 m. It can be seen that as the released height increases, the firebrands have a greater travel distance and wider landing distribution. This is likely due to the higher initial velocity of the boundary layer. Since the boundary layer is defined by an exponential function, the velocity increases as the height increases. It can also be seen that the particle concentration

is higher at 0.25 m and 0.75 m release heights than at 1.25 m and 1.75 m.

Figure 16 shows the aggregate depositions for rod firebrands. It can be seen that the spread of rods is much different than for plates. For rods, their highest concentration is located in one small area across all test trials. As the release height increases, the spread of depositions begins to branch out in the positive X direction, but the highest concentration remains in one location.

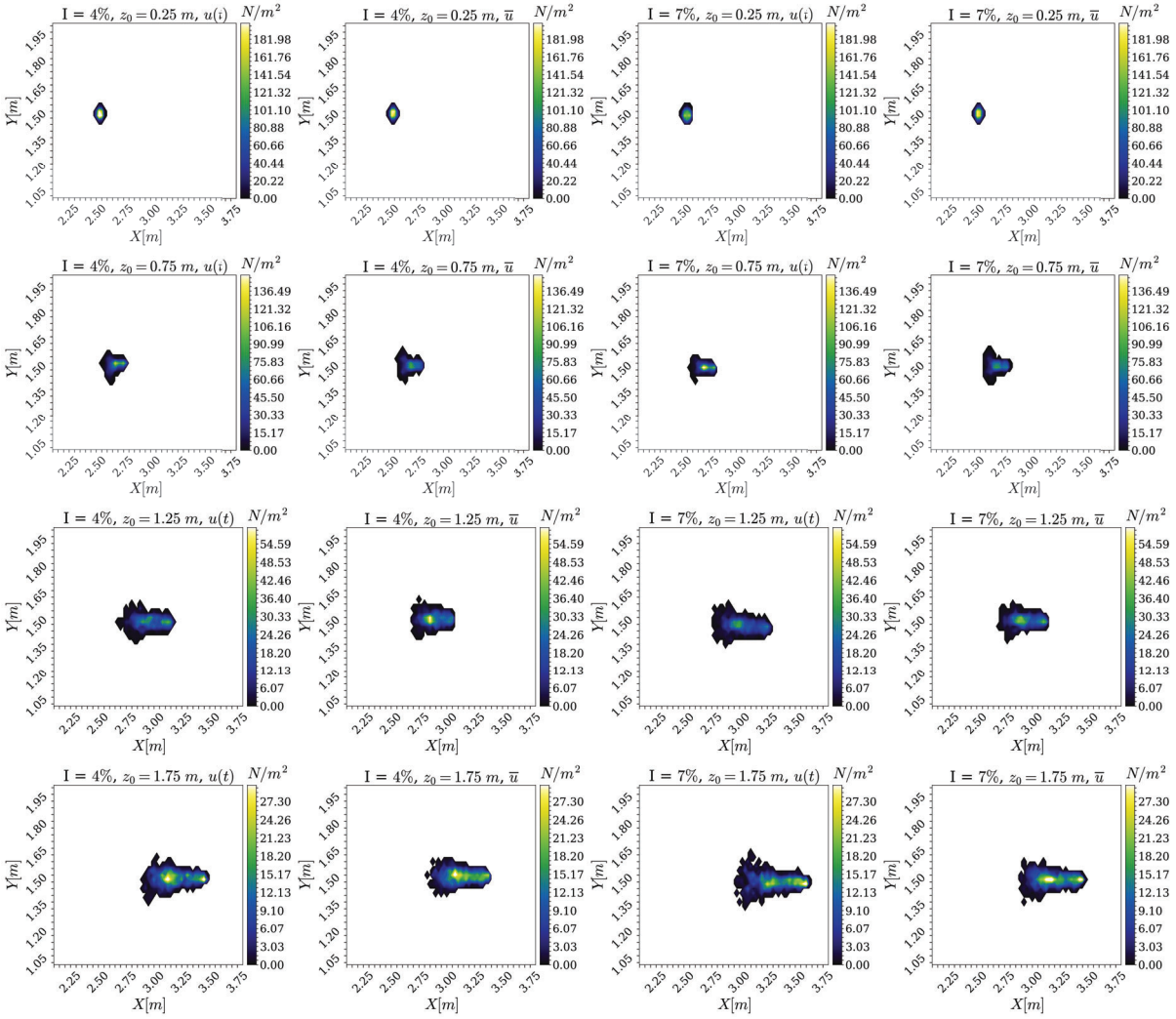

(a) $I = 4\%,\ u(t)$ (b) $I = 4\%,\ \overline{u}$ (c) $I = 7\%,\ u(t)$ (d) $I = 7\%,\ \overline{u}$

Fig. 15. Plate firebrand aggregate deposition count at heights of 0.25 m, 0.75 m, 1.25 m, 1.75 m from top to bottom, and in the instantaneous velocity field of $I = 4\%$ (a), time average velocity field of $I = 4\%$ (b), instantaneous velocity field of $I = 7\%$ (c), and time average velocity field of $I = 7\%$ (d).

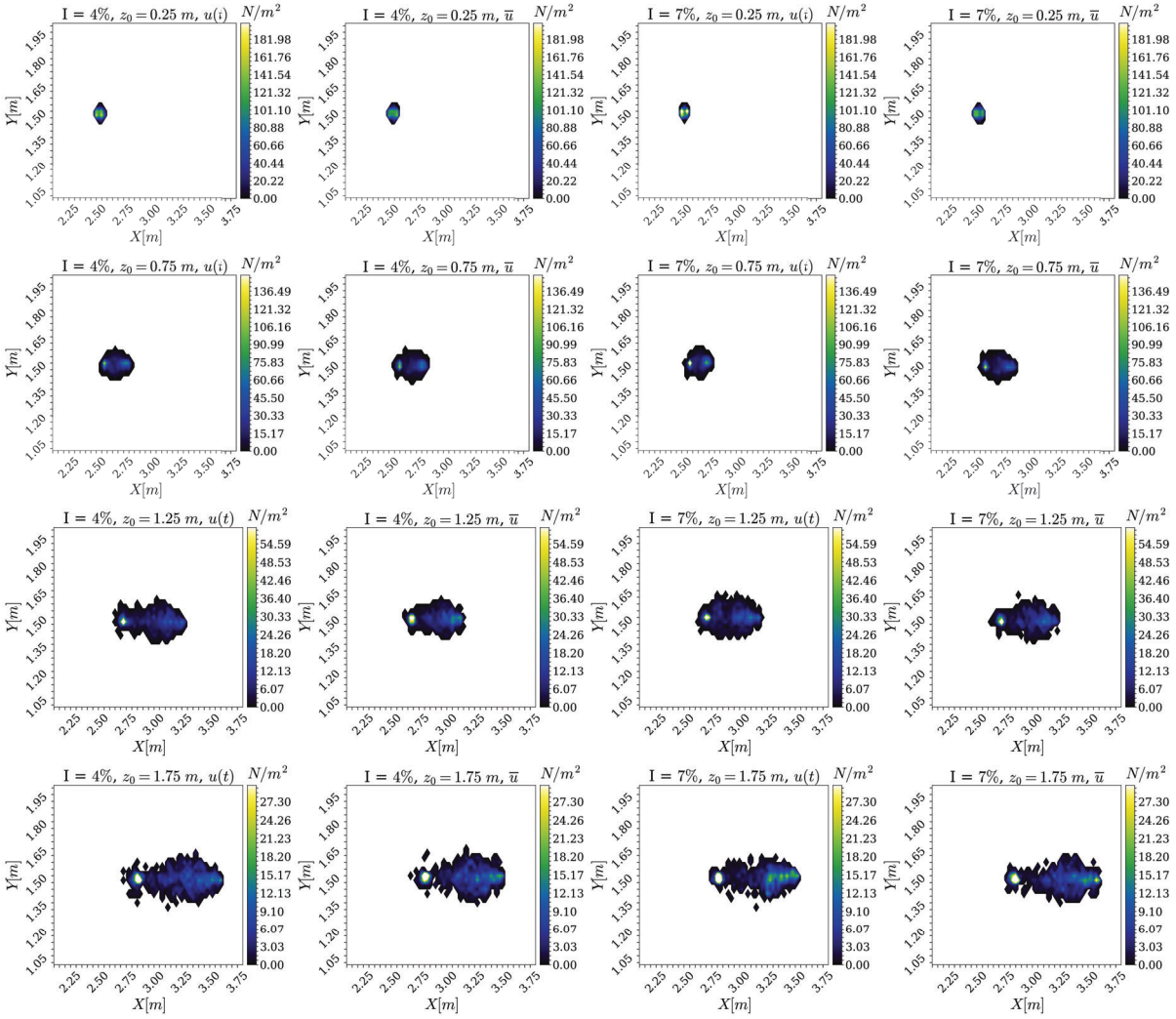

(a) $I = 4\%,\ u(t)$ (b) $I = 4\%,\ \overline{u}$ (c) $I = 7\%,\ u(t)$ (d) $I = 7\%,\ \overline{u}$

Fig. 16. Rod firebrand aggregate deposition count at heights of 0.25 m, 0.75 m, 1.25 m, 1.75 m from top to bottom, and in the instantaneous velocity field of $I = 4\%$ (a), time average velocity field of $I = 4\%$ (b), instantaneous velocity field of $I = 7\%$ (c), and time average velocity field of $I = 7\%$ (d).

5.1.1.2 Travel Distance for $u(t)$ vs $\overline{u}$: The probability density function (PDF) and cumulative density function (CDF) for plate and rod travel distance in the X direction were calculated for all of the small-scale test trials. In Figure 17 and Figure 18, the PDFs and CDFs of the instantaneous and time-averaged velocity fields are compared for the $I = 4\%$ and $I = 7\%$ velocity fields of plates and rods respectively. Plates and rods at release heights 1.25 m and

1.75 m show greater travel distance in the time-averaged velocity field. The PDFs and CDFs of the time-averaged velocity field are shifted further ahead in the positive X direction than the instantaneous field. This finding is similar to the work in Tohidi and Kaye [11], where compact firebrands were found to travel shorter distances in instantaneous velocity fields than time-average velocity fields. The difference in travel distance is only seen in 1.25 m and 1.75 m release heights. In some cases at 0.75 m release height, the instantaneous velocity field has a slightly greater travel distance than time-averaged. At 0.25 m release height, the travel distance is about the same across all test trials. The PDF of rod travel distance is very skewed where the highest probability is closer to the lower end of the travel distance range. This is similar to what is seen in the deposition contour plots which show that the highest concentration of particles land in the same location.

Figure 19 shows the computed average travel distance of plates (top row) and rods (bottom row) in the instantaneous velocity field against the time-averaged with a y=x line to show equality between the two comparisons. In some instances, plates and rods had higher average travel distances in time-averaged velocity fields and instantaneous. Comparing the average travel distance for plates, Figure 19a shows a slight deviation toward the time-averaged velocity field at 1.25 m and 1.75 m release heights, while in Figure 19b shows greater deviation toward the time-averaged velocity field at the same release heights. The average travel distance for plates at 0.25 m and 0.75 m heights in $I = 4\%$ and $I = 7\%$ velocity fields showed that the averages in the instantaneous and time-averaged were nearly equal. Figure 19c shows a slight deviation toward the time-averaged velocity field at release heights 1.25 m and 1.75 m. Figure 19d shows a slight deviation toward the instantaneous velocity field at 0.75 m, 1.25 m, and 1.75 m release heights.

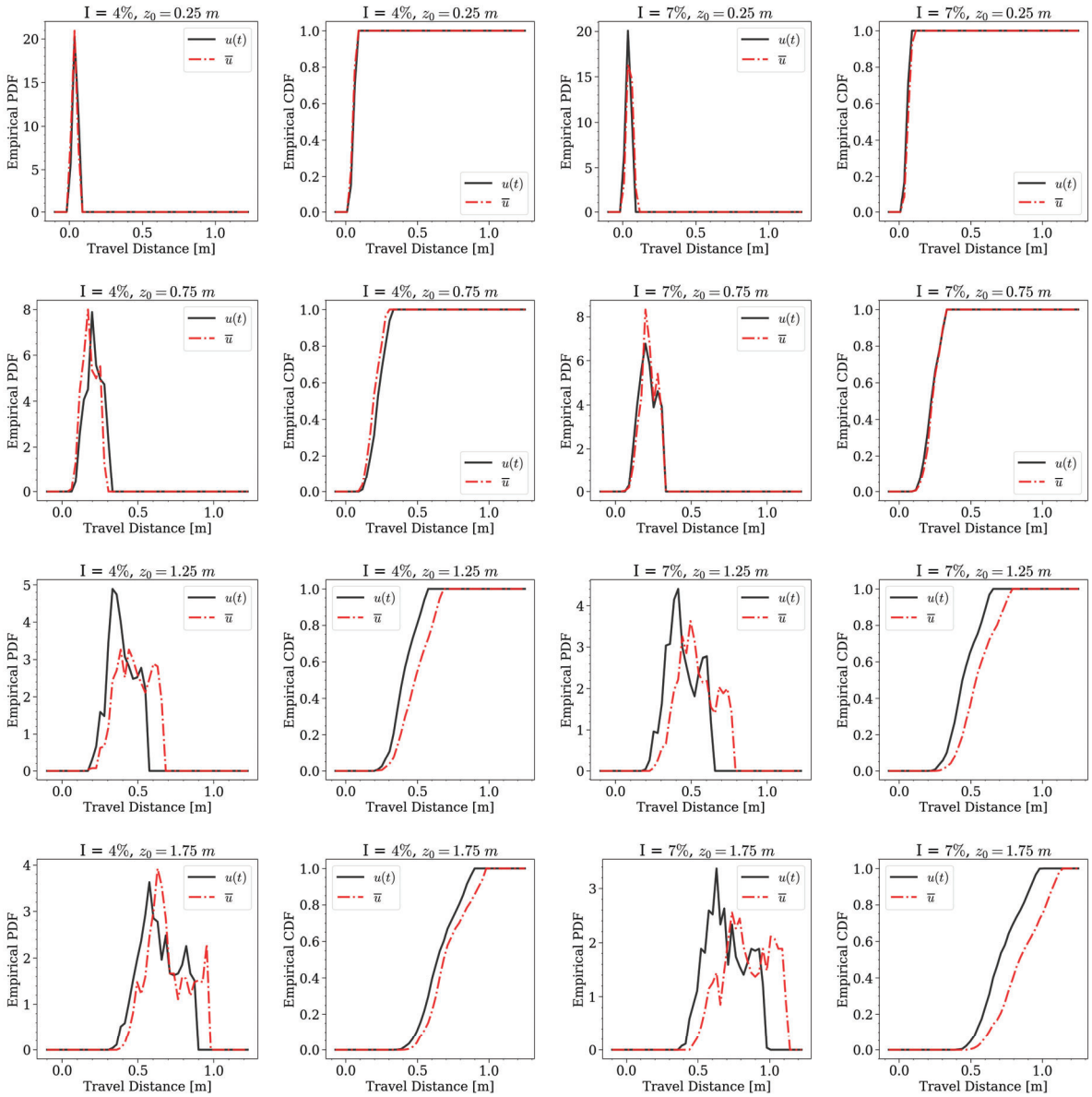

(a) $I = 4\%$, PDF (b) $I = 4\%$, CDF (c) $I = 7\%$, PDF (d) $I = 7\%$, CDF

Fig. 17. Plate firebrand travel distance PDF and CDF at heights of 0.25 m, 0.75 m, 1.25 m, 1.75 m from top to bottom, and at turbulence intensity of 4% PDF (a), turbulence intensity of 4% CDF (b), turbulence intensity of 7% PDF (c), and at turbulence intensity of 4% CDF (d).

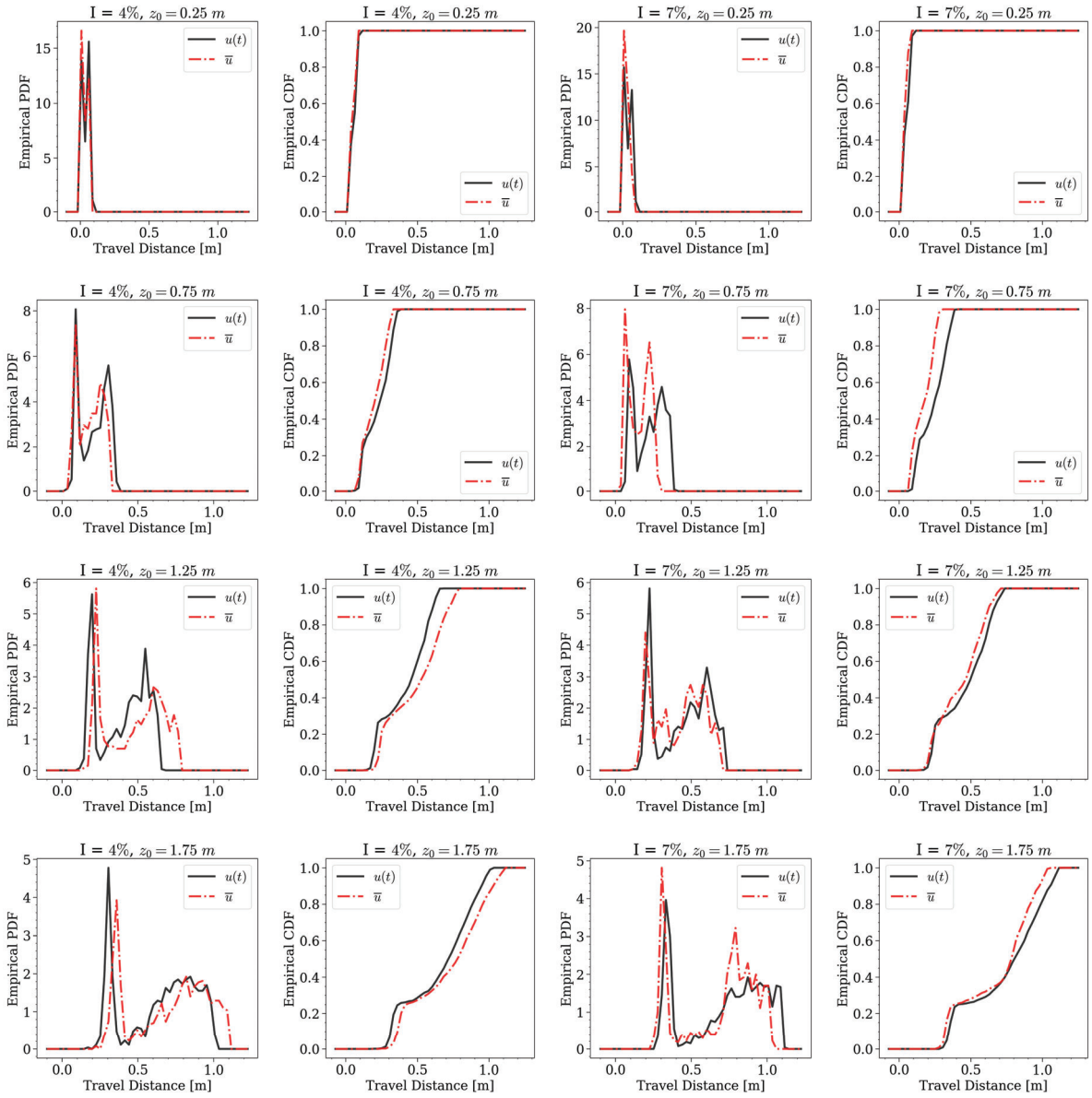

(a) $I = 4\%$, PDF (b) $I = 4\%$, CDF (c) $I = 7\%$, PDF (d) $I = 7\%$, CDF

Fig. 18. Rods firebrand travel distance PDF and CDF at heights of 0.25 m, 0.75 m, 1.25 m, 1.75 m from top to bottom, and at turbulence intensity of 4% PDF (a), turbulence intensity of 4% CDF (b), turbulence intensity of 7% PDF (c), and at turbulence intensity of 4% CDF (d).

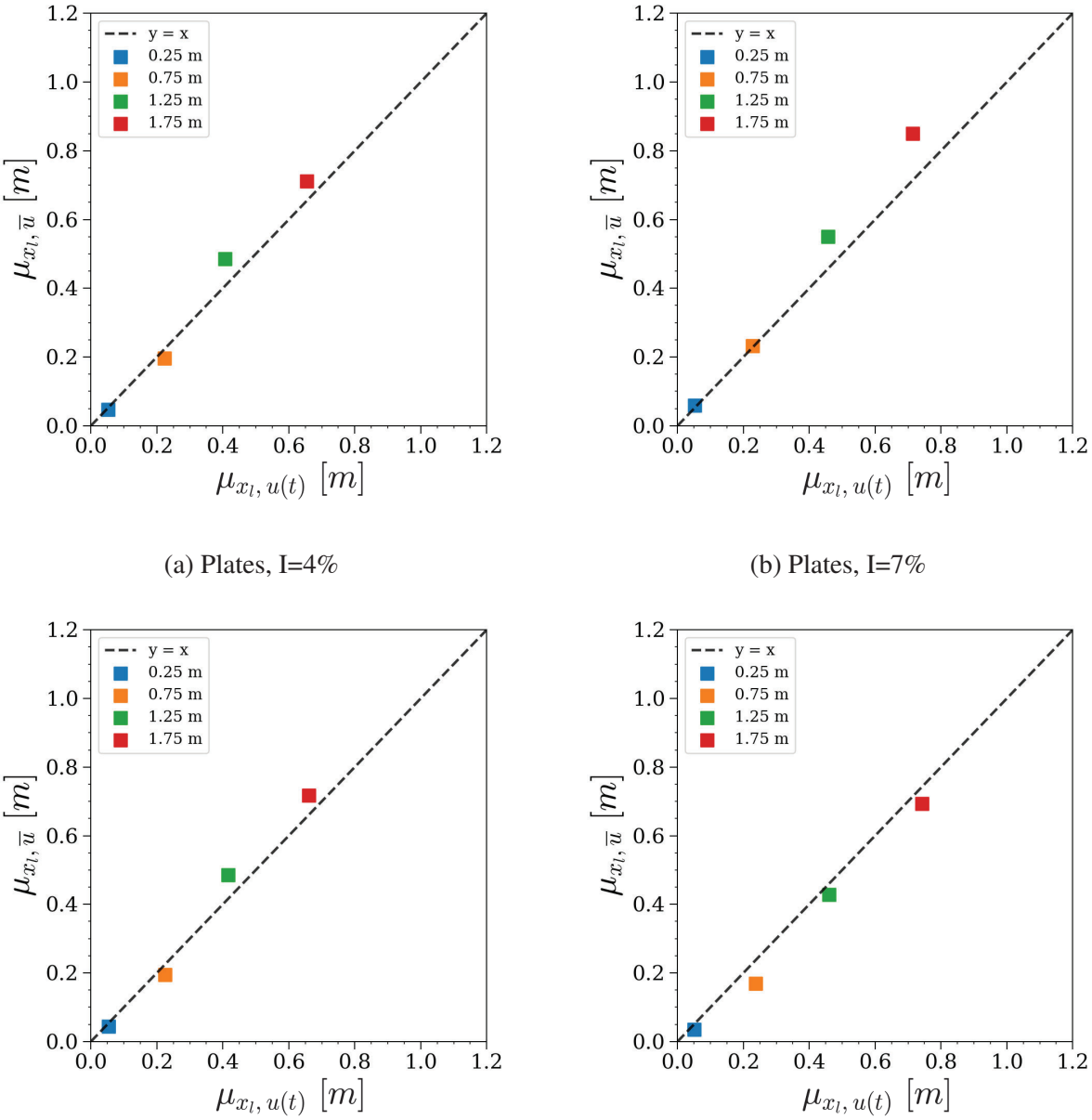

(a) Plates, I=4%

(b) Plates, I=7%

(c) Rods, I=4%

(d) Rods, I=7%

Fig. 19. Average travel distance of plates and rods in instantaneous ($\mu_{x_l,u(t)}$) and time-averaged ($\mu_{x_l,\bar{u}}$) velocity fields at release heights 0.25 m, 0.75 m, 1.25 m, and 1.75 m for plates in 4% (a) and 7% (b) turbulence intensity, and rods in 4% (c) and 7% (d) turbulence intensity.

5.1.1.3 Travel Distance for 4% vs 7% turbulence intensity: The PDF and CDF of the travel distance in the X direction for plates and rods are plotted in Figure 20. These plots show the comparison plate and rod travel distance in $I = 4\%$ and $I = 7\%$ velocity fields. Results show that plates at 1.25 m and 1.75 m release heights had greater travel distance in $I = 7\%$, and rods at 1.25 m and 1.75 m release heights had a slighty greater travel distance in $I = 4\%$. For both plates and rods, the difference in PDF travel distance is lower at 0.25 m and 0.75 m release heights. The difference in the PDF travel distance for rods at 1.25 m and 1.75 m release heights is smaller than for plates, which means that plates are more sensitive to change in turbulence intensity. This is likely due to a higher turbulent kinetic energy (TKE) in the 7% turbulence intensity case. The TKE may have a greater effect on the plate particles than the rod particles. Since the frontal area of the l_y and l_z face for plates is larger, when oriented normal to the wind vector, can cause a greater drag force on plates than on rods.

Figure 21 shows the average travel distance for plates and rods in the $I = 4\%$ and $I = 7\%$ velocity fields. Results show that the average travel distance of plates at heights 1.25 m and 1.75 m deviate more towards the $I = 7\%$. Rods show a small deviation toward $I = 4\%$ at 0.75 m release height. This verifies that turbulence intensity had a greater effect on plates than rods.

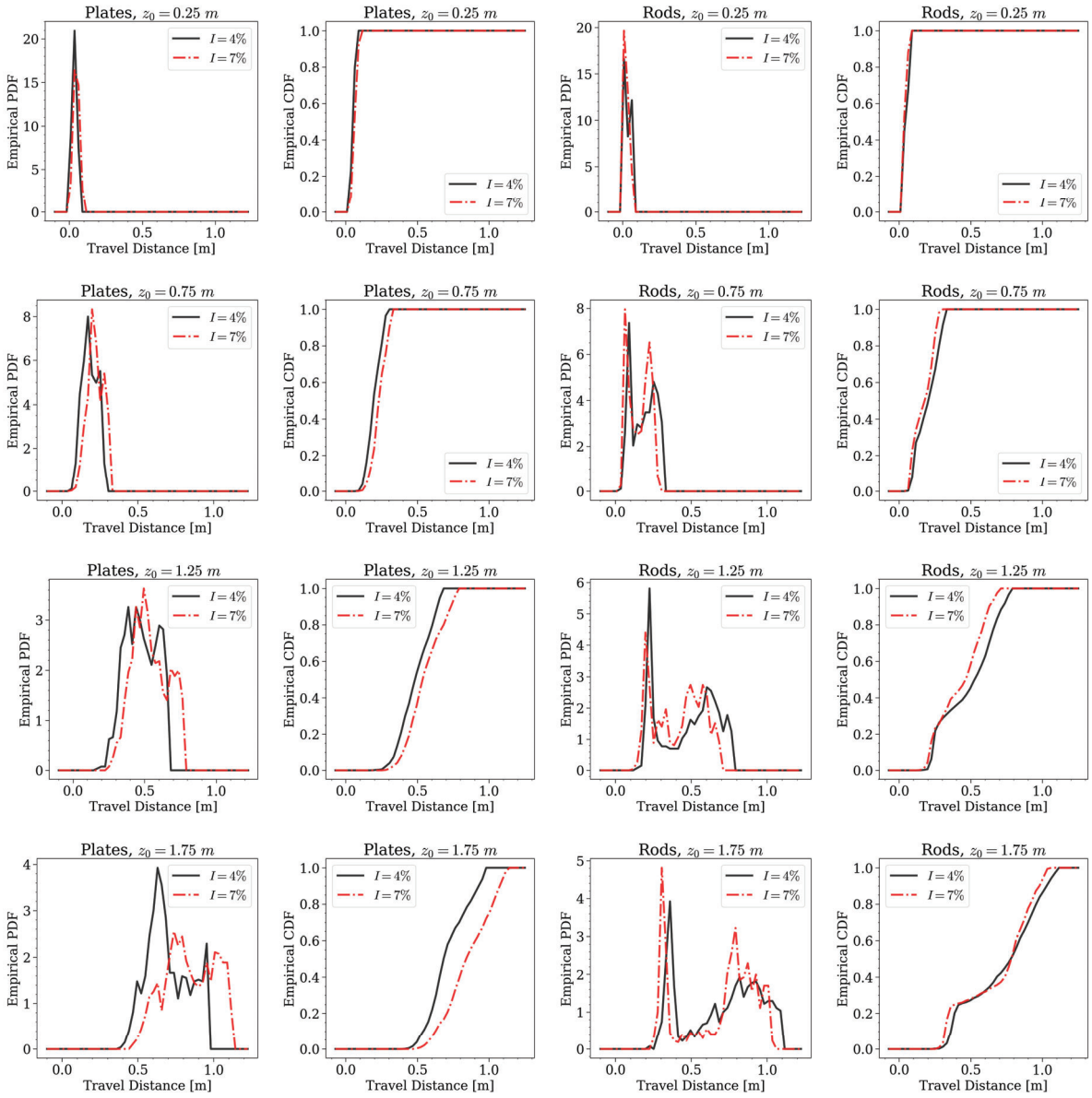

(a) Plates PDF (b) Plates CDF (c) Rods PDF (d) Rods CDF

Fig. 20. Comparison of plate and rod travel distance in 4% and 7% turbulence intensity at heights of of 0.25 m, 0.75 m, 1.25 m, 1.75 m from top to bottom for plates PDF (a), plates CDF (b), rods PDF (c), rods CDF (c).

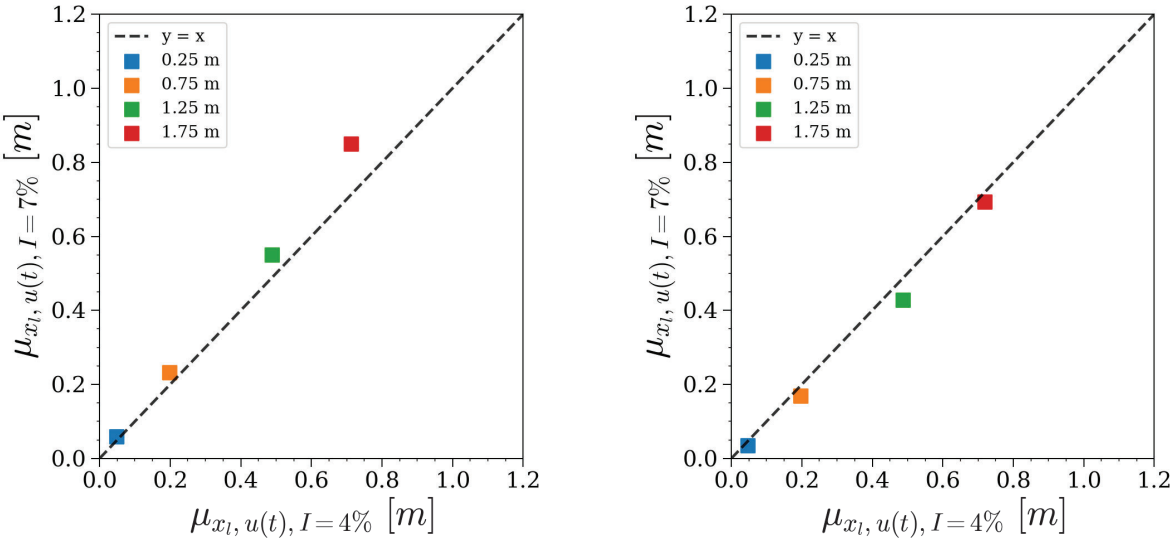

(a) Plates PDF

(b) Plates CDF

Fig. 21. Average travel distance of plates (a) and rods (b) in 4% turbulence intensity ($\mu_{x_l,u(t),I=4\%}$) and 7% turbulence intensity ($\mu_{x_l,u(t),I=7\%}$) velocity fields at release heights 0.25 m, 0.75 m, 1.25 m, and 1.75 m.

5.2 Large-scale Firebrand Transport

Simulations for large-scale firebrand transport used particles with fixed dimensions of $l_x =$ 3 mm, $l_y = 15$ mm, $l_z = 25$ mm for plates, and $l_x = 3$ mm, $l_y = 5$ mm, $l_z = 25$ mm for rods. The density of each firebrand was set to 300 kg/m^3 to represent the poplar wood species. This gave a fixed mass of 3.38×10^{-7} kg for plates and 1.12×10^{-7} kg for rods. A total of 100 firebrands were released at each timestamp in the area of active fire from the WRF-SFIRE simulations. The Manning Creek simulation contained 100 timesteps, each being 15 minutes apart. This resulted in 10,000 firebrands released throughout the entire duration of the transport simulation. The Creek Fire simulation contained 109 timesteps, each being 10 minutes apart. This resulted in 10,900 firebrands released throughout the simulation duration. The number of particles released at each timestep was an arbitrary value set to test the transport of firebrands

in large-scale domains. The release height of each initialized particle ranged from 2-10 m on a uniform random distribution. This was also set as an arbitrary range to test varying heights in the boundary layer of the WRF-SFIRE domain. All particles were oriented from 0-2π on all 3 of its principal axes selected from a uniform random distribution.

5.2.1 Results

5.2.1.1 Particle Depositions: The landing distribution of firebrands in the WRF-SFIRE domains was calculated by a summation of depositions over a 1x1 m^2 area. The landing distribution of firebrands is visualized as a time series in Figure 22 for plates and in Figure 23 for rods from the Manning Creek simulation. The depositions and perimeter of the fire line are plotted at each timestamp and show the progression of the fire and particle depositions. It can be seen that the fire grows outward in all directions, along with firebrand depositions. Although the Manning Creek simulation is a high wind speed case (Re=5,170,572), a majority of the depositions are close to the fire perimeter. The plate and rod particles have similar landing distributions throughout the simulation. The landing distribution time series for the Creek Fire simulation is seen in Figure 24 for plates and Figure 25 for rods. In these simulations, there are depositions far outside of the fire perimeter. In the Creek Fire case, there were spot fires simulated in WRF-SFIRE, and it can be seen that the firebrands land near the same locations as the simulated spot fires. Both plates and rods have similar landing distributions, however, some plate particles have larger travel distances.

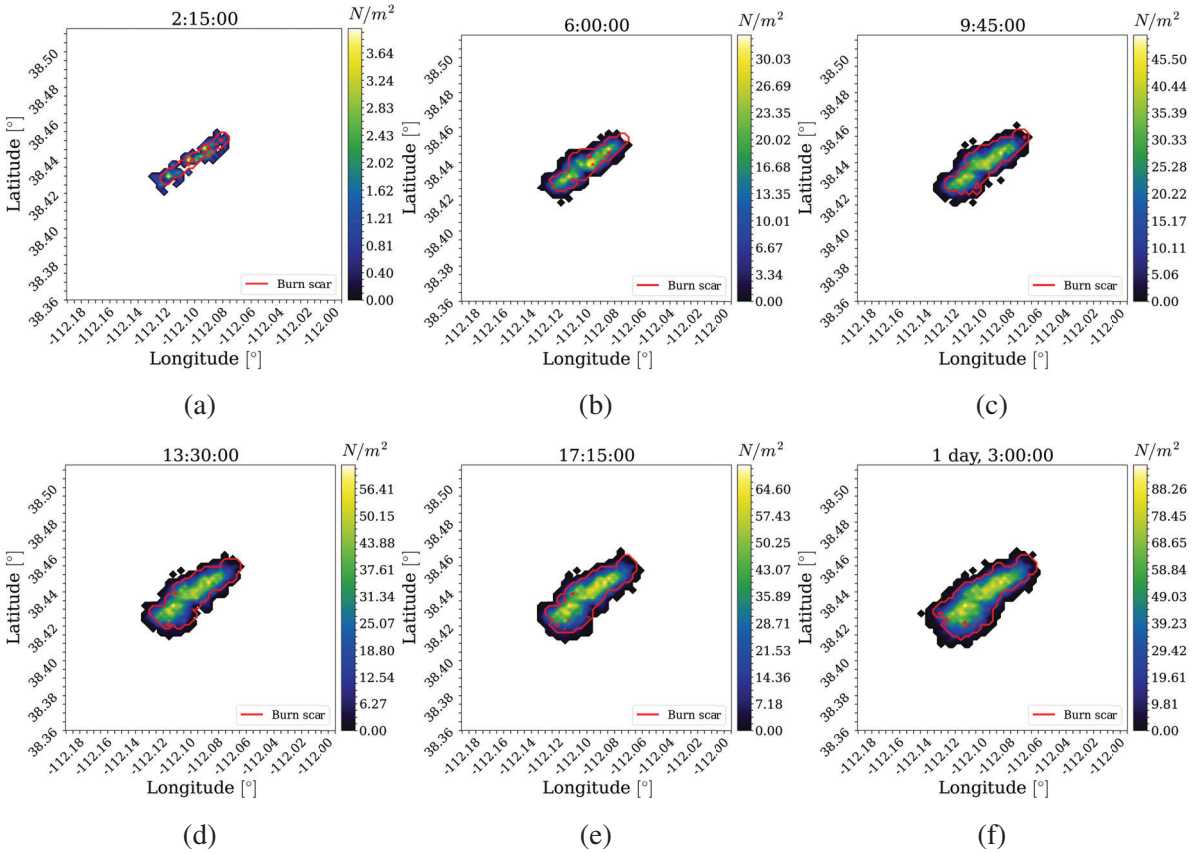

Fig. 22. Firebrand landing distribution time series of plates in WRF-SFIRE Manning Creek simulation. The landing distribution and burn scar are from the time indicated at the top of the plot.

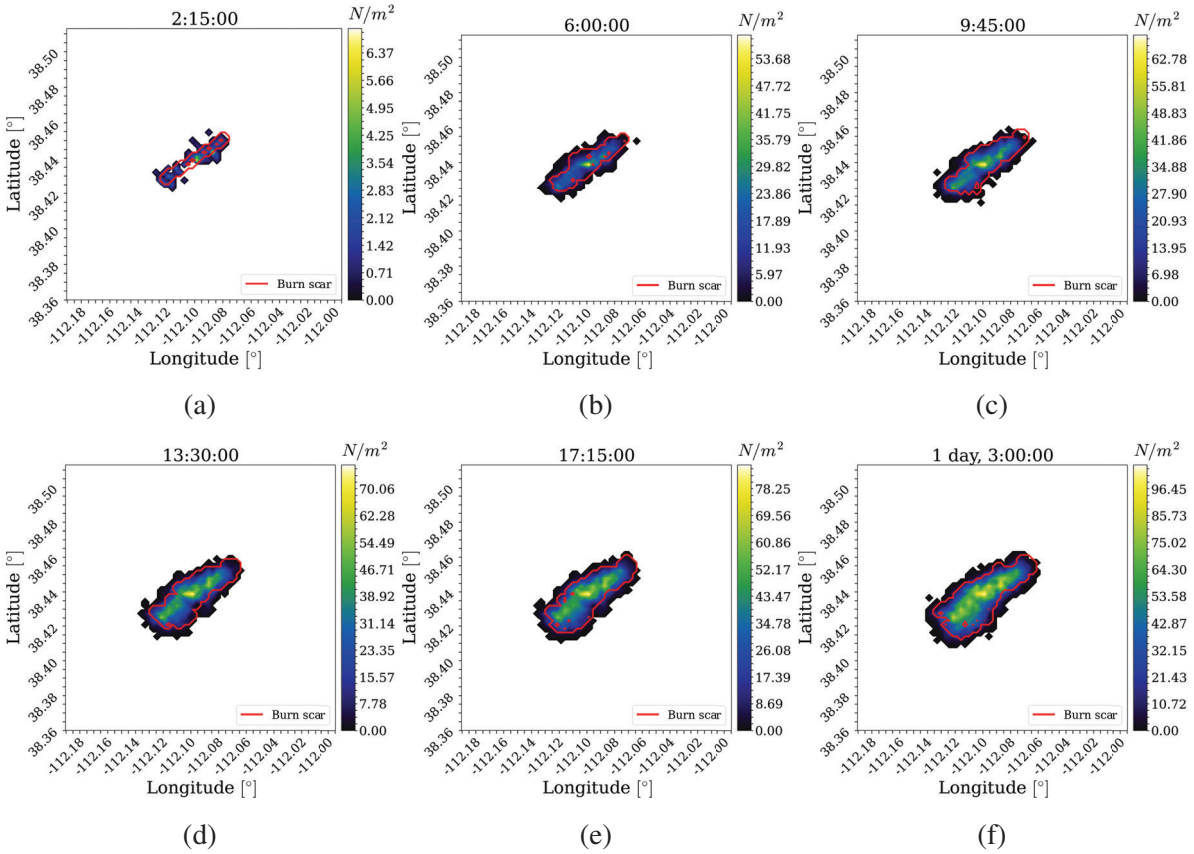

Fig. 23. Firebrand landing distribution time series of rods in WRF-SFIRE Manning Creek simulation. The landing distribution and burn scar are from the time indicated at the top of the plot.

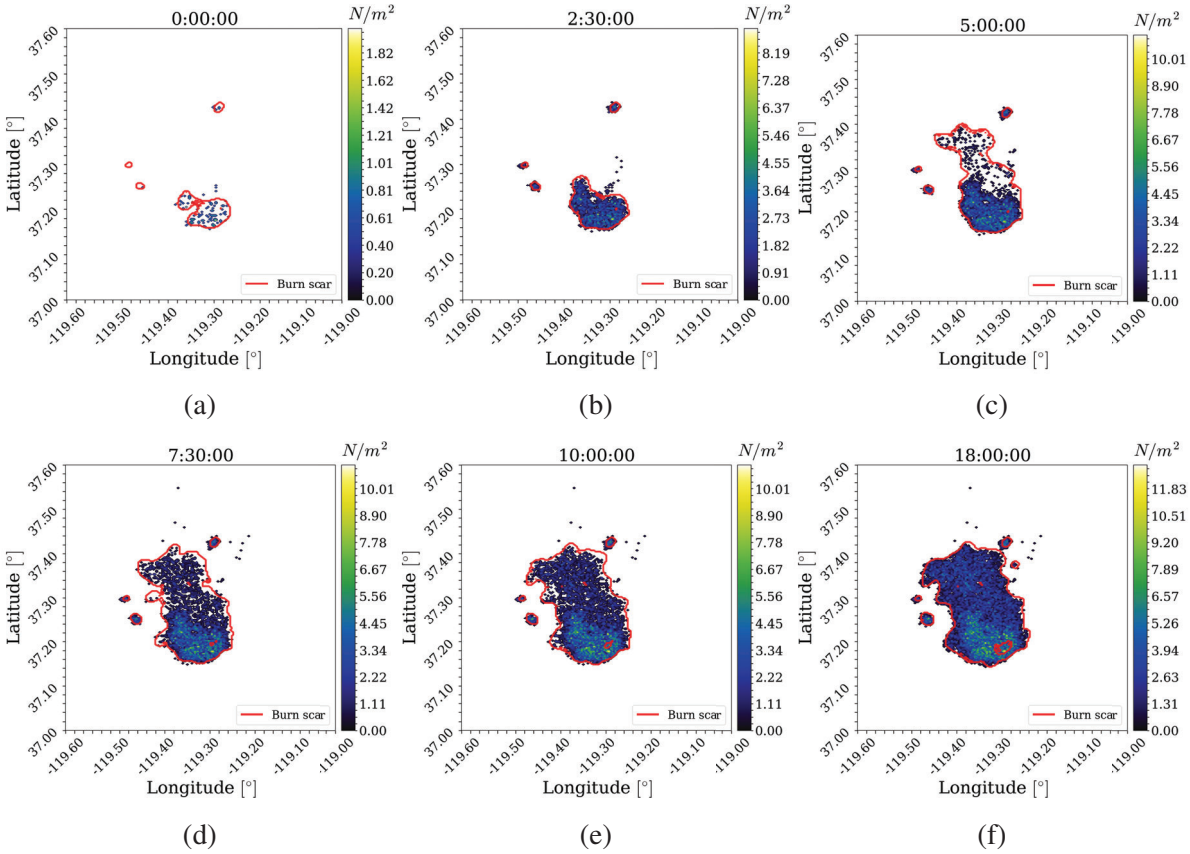

Fig. 24. Firebrand landing distribution time series of plates in WRF-SFIRE Creek Fire simulation. The landing distribution and burn scar are from the time indicated at the top of the plot.

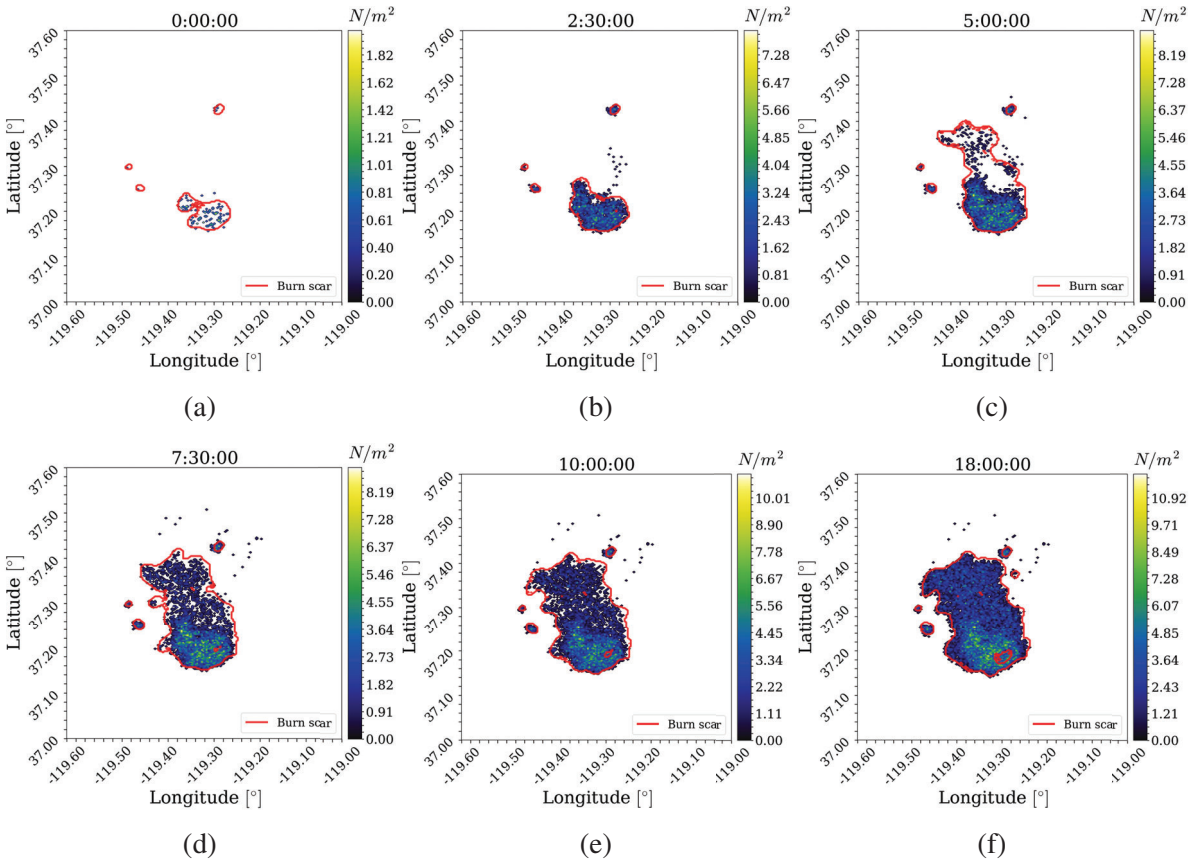

Fig. 25. Firebrand landing distribution time series of rods in WRF-SFIRE Creek Fire simulation. The landing distribution and burn scar are from the time indicated at the top of the plot.

5.2.1.2 Travel Distance: The travel distance of firebrands in the Manning Creek and Creek Fire simulation was calculated using the distance formula (5):

$$R = \sqrt{(x_2 - x_1)^2 + (y_2 - y_1)^2} \tag{5}$$

were (x_1, y_1) is the initial location of the firebrand and (x_2, y_2) is the final location of the firebrand. The average and maximum travel distance is seen in Table 4. Plates and rods had higher average travel distances in the Creek Fire simulation. Rods were found to have higher average travel distances than plates in both Manning Creek and Creek Fire simulations. Rods

were found to have the farthest travel distance of 2364 m in the Manning Creek simulation, while plates had the farthest of 31559 m in the Creek Fire simulation.

Table 4
Average and Maximum Travel Distance

Simulation Case	**Plates**		**Rods**	
	μ_R [m]	R_{max} [m]	μ_R [m]	R_{max} [m]
Manning Creek	31.52	1899.78	41.13	2363.89
Creek Fire	57.14	31558.99	76.09	27417.81

The empirical PDFs of plate and rod travel distance are calculated using 100 bins and a range of 0 to 50. The range was set to show the difference in probability between the various simulation cases. Figure 26 shows a comparison of the empirical PDF of plates versus rods in the Manning Creek (26a) and Creek Fire (26b) simulations. The travel distances of plates and rods are very similar in both Manning Creek and Creek Fire, and the peak probability is nearly the same in both cases. Figure 27 shows a comparison of the empirical PDF of Manning Creek versus Creek Fire simulations for plates (27a) and rods (27b). The travel distance of plates and rods is farther in the Creek Fire simulation than in the Manning Creek simulation.

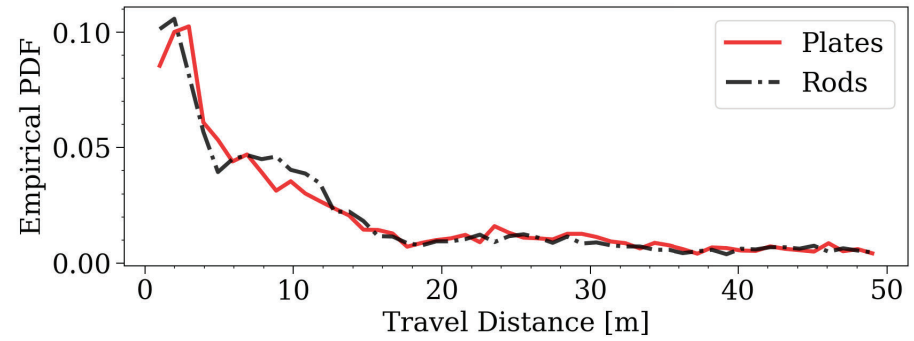

(a)

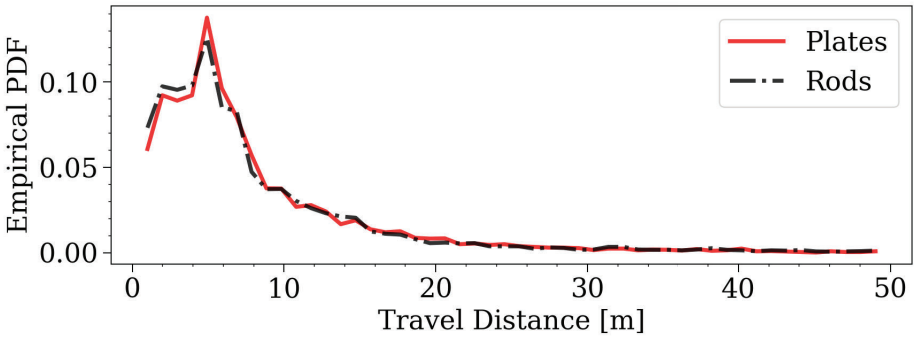

(b)

Fig. 26. Empirical PDF of firebrand travel distance comparison of plates versus rods in Manning Creek (a) and Creek Fire (b) simulations.

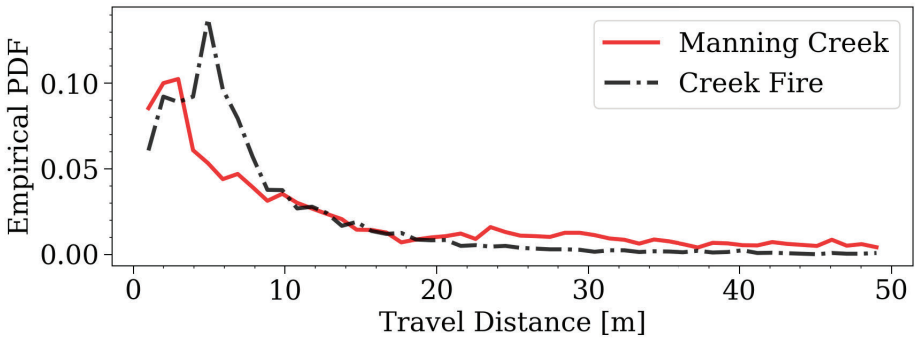

(a)

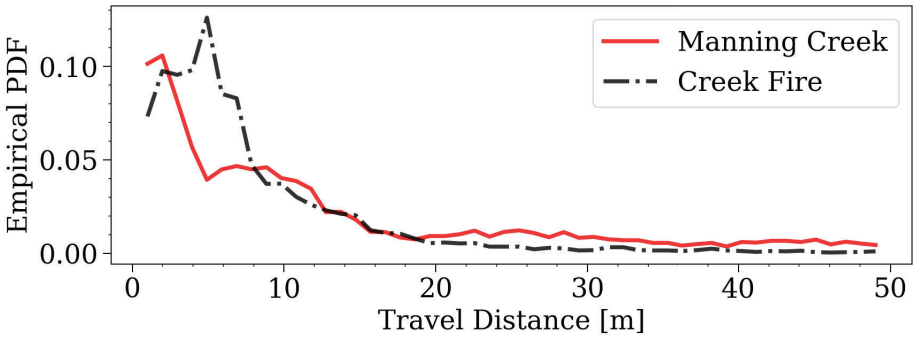

(b)

Fig. 27. Empirical PDF of firebrand travel distance comparison of Manning Creek versus Creek Fire simulations for plates (a) and rods (b).

5.2.1.3 Particle Trajectories: The firebrand trajectories in the Manning Creek simulation are shown in figures 28 for plates and 29 for rods. Due to high winds in the Manning Creek simulation, the smoke plume is highly bent over, resulting in little vertical lofting. This causes minimal downwind transport. The opposite is seen in the Creek Fire simulation, seen in Figures 30 for plates and 31 for rods, which shows high vertical lofting and large downwind transport. Since the wind speeds are low in the Creek Fire simulation, a more vertical smoke plume is formed, allowing the firebrands to be lofted upwards. A similar finding is seen in the small-scale transport data, where the firebrands have greater travel distances as their release height increases.

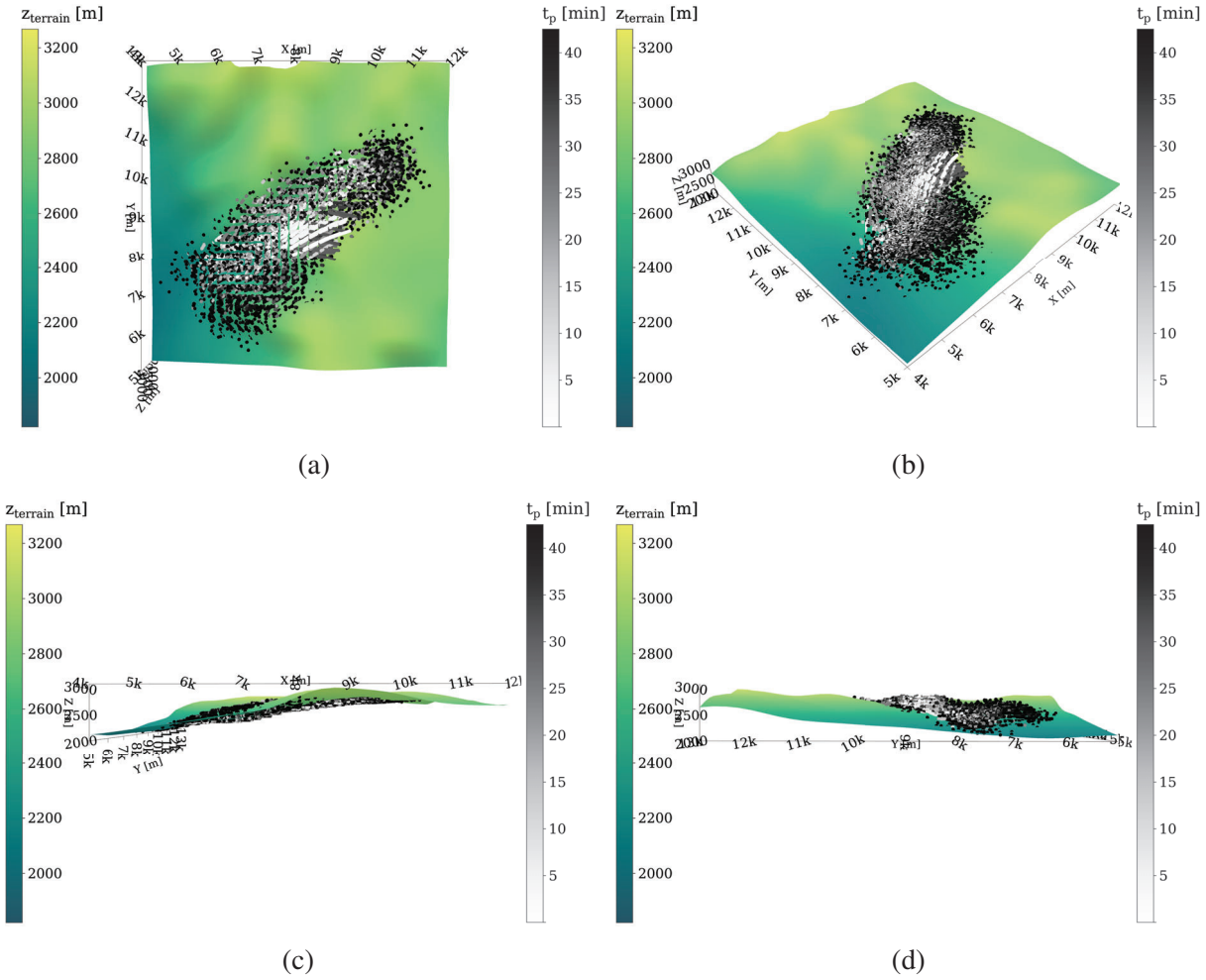

Fig. 28. Firebrand trajectories of plate particles and terrain topography of Manning Creek wildfire case. Particles are colored by simulation time and terrain by elevation height. 3D orientations of XY (a), isometric (b), XZ (c), YZ (d) views.

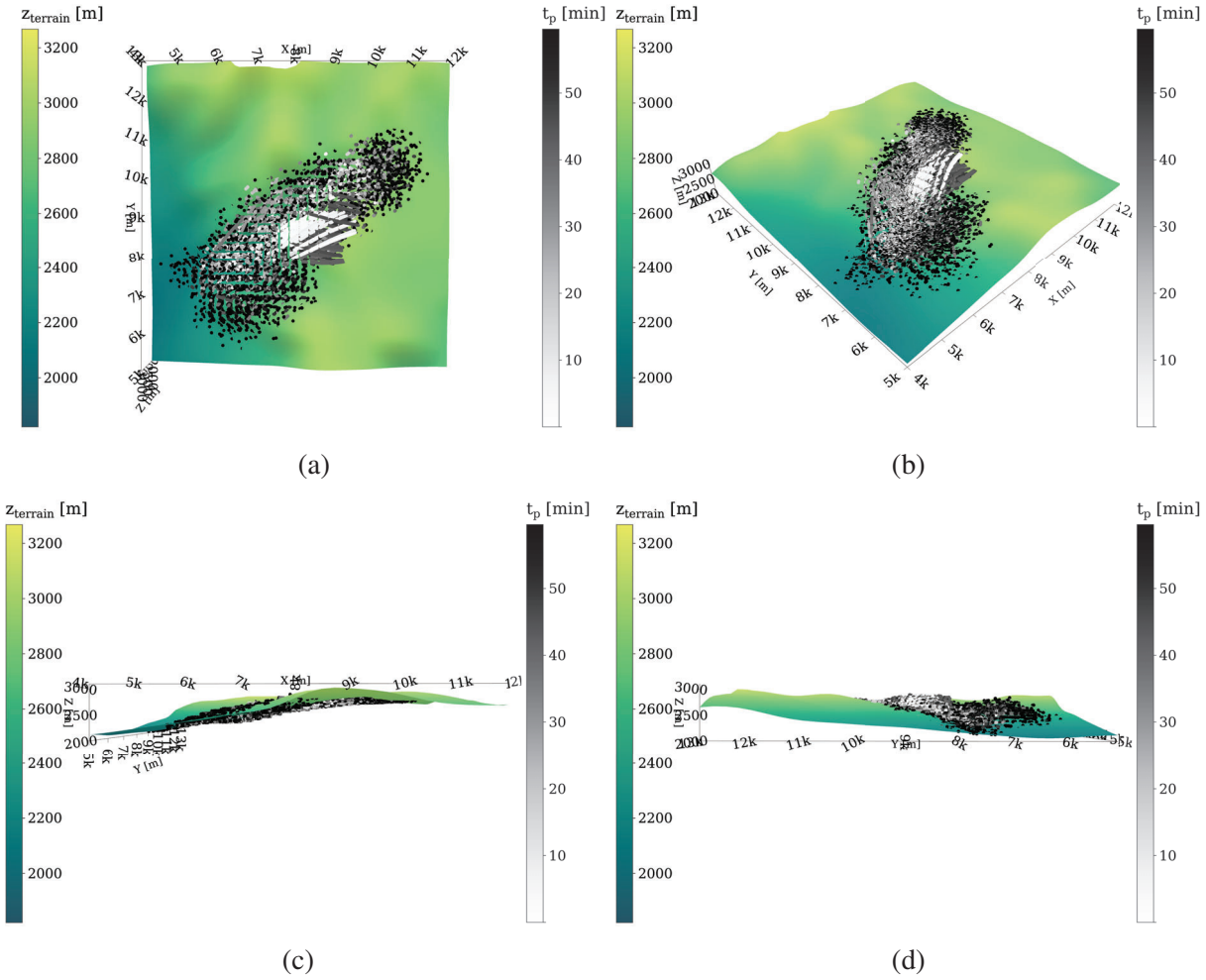

Fig. 29. Firebrand trajectories of rod particles and terrain topography of Manning Creek wildfire case. Particles are colored by simulation time and terrain by elevation height. 3D orientations of XY (a), isometric (b), XZ (c), YZ (d) views.

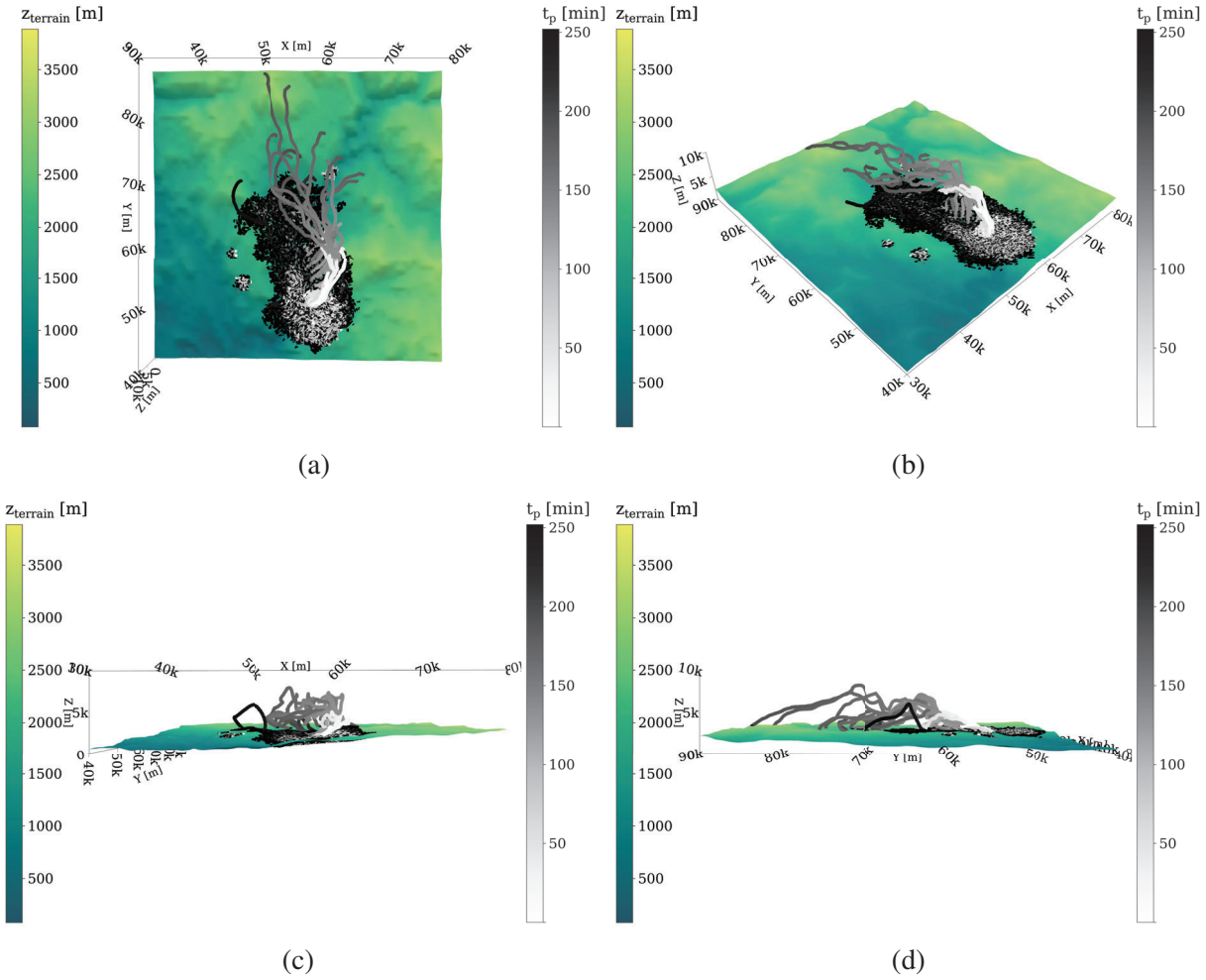

Fig. 30. Firebrand trajectories of plate particles and terrain topography of Creek Fire wildfire case. Particles are colored by simulation time and terrain by elevation height. 3D orientations of XY (a), isometric (b), XZ (c), YZ (d) views.

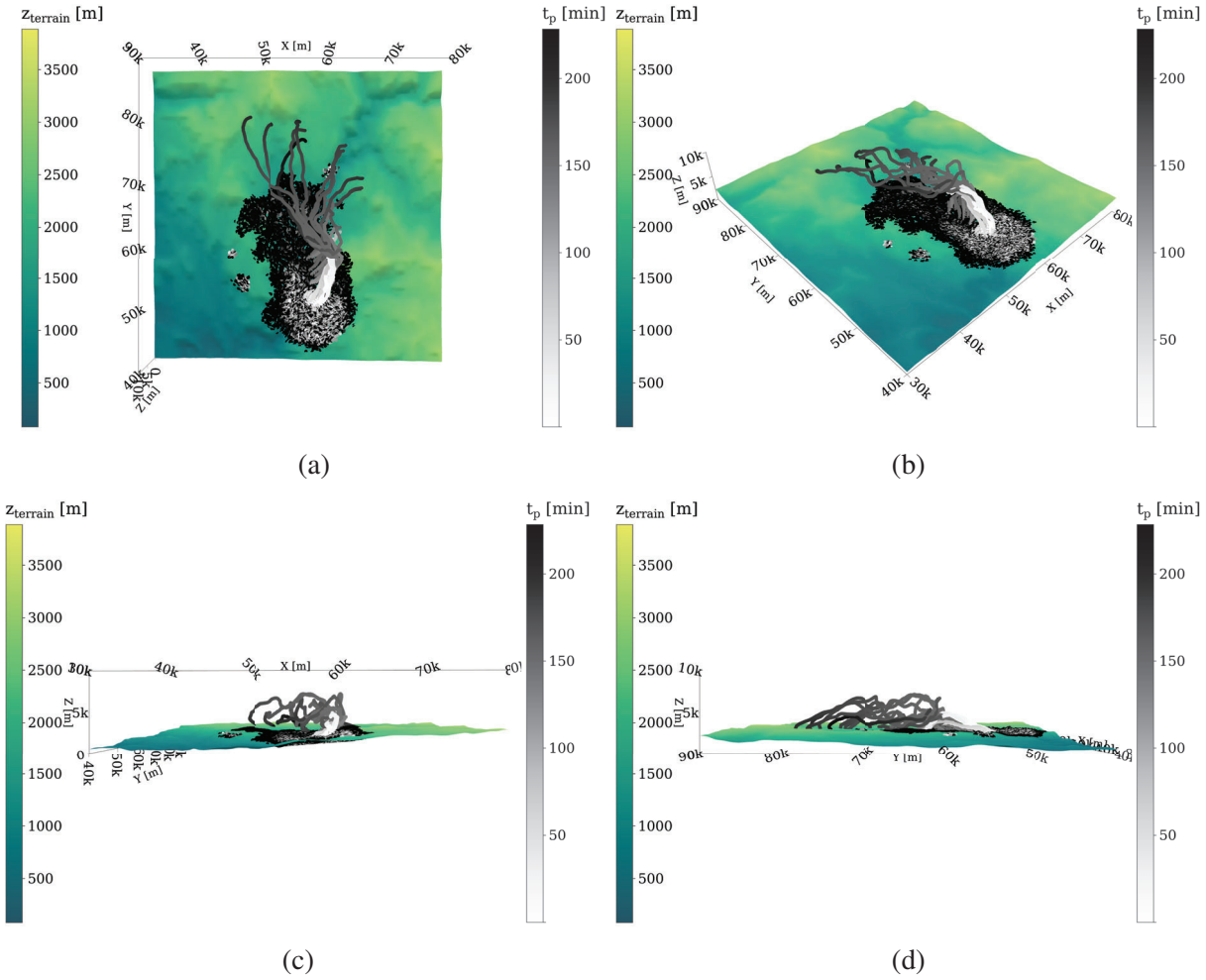

Fig. 31. Firebrand trajectories of rod particles and terrain topography of Creek Fire wildfire case. Particles are colored by simulation time and terrain by elevation height. 3D orientations of XY (a), isometric (b), XZ (c), YZ (d) views.

6 CONCLUSIONS

6.1 Summary & Significant Findings

The effect of small-scale turbulence on firebrand landing distribution was studied. High-resolution turbulent boundary layers were simulated at two turbulence intensities and validated for numerical experiments. Firebrands shaped as plates and rods were released in turbulent and uniform flows at four different heights. The landing distribution of plates was found to be significantly different from rods. Plates had a high concentration of depositions over a large area, while rods had a high concentration over a small area. The transport of plates and rods in uniform flows led to over-predicted travel distances in contrast to those in turbulent flows. Plates were found to have more sensitivity to changes in turbulence intensity than rods. These results give considerable implications that the shape of the firebrand affects landing distribution.

The firebrand transport solver was two-way coupled with WRF-SFIRE for large-scale transport of plates and rods. The coupling methodology uses a staggered data-sharing scheme that reads velocity and fire data and feeds back firebrand depositions forward in time. The results of the large-scale transport simulations showed that firebrands have high travel distances in low Reynold's numbers and low travel distances in high Reynold's numbers. This is likely due to the fact that fire plumes are more bent over at high wind speeds which causes the firebrands to have less vertical lofting. The landing distribution and travel distance PDFs of plates and rods were observed to be similar in the high wind speed case and the low wind speed case. This does not match the small-scale transport results which showed that the landing distribution and travel distances differed between plates and rods. This indicates that the absence of small-scale turbulence in large-scale wildfire domains may have an effect on where firebrands land. Firebrands were found to travel large distances up to 30,000 m. This is dangerous because firebrands could potentially travel across any barriers set up by firefighters, and ignite

spot fires far from the main firefront. The surrounding areas of a wildfire could have spot fire ignitions in numerous locations, and communities located near the active wildfire are at risk of spot fire ignitions.

6.2 Future Work Recommendations

Improved wildfire simulations with spot fire ignitions could aid researchers in understanding the firebrand shower phenomena and how wildfires spread. This knowledge could be passed on to firefighters who will be better equipped to fight and suppress wildfires against dangerous wildfires and save communities. Continued work in firebrand transport simulations is a necessity. More tests are needed with varying firebrand shapes, sizes, and densities. The implementation of firebrand thermodynamics should be studied for the analysis of heat energy upon deposition and its risk of spot fire ignition. More WRF-SFIRE simulations with various topographies, wind conditions, and fire progressions are needed. Further tests are needed to verify the difference in firebrand transport in small-scale and large-scale turbulence domains. A fully coupled firebrand transport wildfire simulation is also needed to fully understand how wildfires behave with spot fires generated from computed trajectories.

Future applications of this work could be to implement a data-driven model to predict the landing locations of plate and rod firebrands. With more simulation results of various firebrand shapes and sizes, predictions could be made from based on the initial wind velocity, turbulent kinetic energy, particle location, and more. Moving toward a data-driven model could increase the computational speed of the firebrand transport model.

LITERATURE CITED

[1] "National interagency coordination center wildland fire summary and statistics annual report 2021," National Interagency Coordination Center, Tech. Rep., 2021.

[2] S. Manzello, "Enabling the investigation of structure vulnerabilities to wind- driven firebrand showers in wildland-urban interface (WUI) fires," *Fire Saf. Sci.*, vol. 11, pp. 83–96, 2014.

[3] A. Tohidi, "Experimental and numerical modeling of wildfire spread via fire spotting," Ph.D. dissertation, Dept. Civ. Eng., Clemson Univ., Clemson, SC, USA, 2016.

[4] N. Sardoy, J. L. Consalvi, A. Kaiss, A. C. Fernandez-Pello, and B. Porterie, "Numerical study of ground-level distribution of firebrands generated by line fires," *Combust. Flame*, vol. 154, no. 3, pp. 478–488, Aug. 2008.

[5] H.-H. Wang, "Analysis on downwind distribution of firebrands sourced from a wildland fire," *Fire Technol.*, vol. 47, no. 2, pp. 321–340, Apr. 2011.

[6] A. Mankame and B. Shotorban, "Deposition characteristics of firebrands on and around rectangular cubic structures," *Front. Mech. Eng. Chin.*, vol. 7, 2021.

[7] W. Mell, A. Maranghides, R. McDermott, and S. L. Manzello, "Numerical simulation and experiments of burning douglas fir trees," *Combust. Flame*, vol. 156, no. 10, pp. 2023–2041, Oct. 2009.

[8] E. Koo, R. R. Linn, P. J. Pagni, and C. B. Edminster, "Modelling firebrand transport in wildfires using HIGRAD/FIRETEC," *Int. J. Wildland Fire*, vol. 21, no. 4, pp. 396–417, Mar. 2012.

[9] T. F. Fric and A. Roshko, "Vortical structure in the wake of a transverse jet," *J. Fluid Mech.*, vol. 279, pp. 1–47, Nov. 1994.

[10] S. H. Smith and M. G. Mungal, "Mixing, structure and scaling of the jet in crossflow," *J. Fluid Mech.*, vol. 357, pp. 83–122, Feb. 1998.

[11] A. Tohidi and N. B. Kaye, "The sensitivity of modeled flight distance to the lofting to transport transition criterion in coupled ember flight models," *12th Americas Conference on Wind Engineering 2013, ACWE 2013: Wind Effects on Structures, Communities, and Energy Generation*, pp. 433–448, Dec. 2013.

[12] N. Sardoy, J.-L. Consalvi, B. Porterie, and A. C. Fernandez-Pello, "Modeling transport and combustion of firebrands from burning trees," *Combust. Flame*, vol. 150, no. 3, pp. 151–169, Aug. 2007.

[13] E. Koo, P. J. Pagni, D. R. Weise, and J. P. Woycheese, "Firebrands and spotting ignition in large-scale fires," *Int. J. Wildland Fire*, vol. 19, no. 7, pp. 818–843, Nov. 2010.

[14] P. J. Richards, N. Williams, B. Laing, M. McCarty, and M. Pond, "Numerical calculation of the three-dimensional motion of wind-borne debris," *J. Wind Eng. Ind. Aerodyn.*, vol. 96, no. 10, pp. 2188–2202, Oct. 2008.

[15] P. J. Richards, "Steady aerodynamics of rod and plate type debris," in *Proceedings of the Seventeenth Australasian Fluid Mechanics Conference,* (Auckland, New Zealand), vol. 5, 2010, pp. 222–225.

[16] M. Grayson, W. Pang, and S. Schiff, "Three-dimensional probabilistic wind-borne debris trajectory model for building envelope impact risk assessment," *J. Wind Eng. Ind. Aerodyn.*, vol. 102, pp. 22–35, Mar. 2012.

[17] J. M. Grayson, "Development and Application of a Three-dimensional Probabalistic Wind-borne Debris Trajectory Model," M.S. thesis, Dept. Civ. Eng., Clemson Univ., Clemson, SC, USA, 2011.

[18] S. B. Pope, *Turbulent Flows*. Cambridge, NY: USA: Cambridge University Press, 2000.

[19] J. Mandel, M. Vejmelka, A. Kochanski, *et al.*, "An interactive Data-Driven HPC system for forecasting weather, wildland fire, and smoke," in *2019 IEEE/ACM HPC for Urgent Decision Making (UrgentHPC)*, Nov. 2019, pp. 35–44.

[20] S. L. Manzello, J. R. Shields, T. G. Cleary, *et al.*, "On the development and characterization of a firebrand generator," *Fire Saf. J.*, vol. 43, no. 4, pp. 258–268, May 2008.

[21] S. L. Manzello, A. Maranghides, and W. E. Mell, "Firebrand generation from burning vegetation," *Int. J. Wildland Fire*, vol. 16, no. 4, p. 458, 2007.

[22] S. L. Manzello, A. Maranghides, J. R. Shields, W. E. Mell, Y. Hayashi, and D. Nii, "Mass and size distribution of firebrands generated from burning korean pine (pinus koraiensis) trees," *Fire Mater.*, vol. 33, no. 1, pp. 21–31, Jan. 2009.

[23] J. L. Junkins and H. Schaub, *Analytical Mechanics of Space Systems, Second Edition* (AIAA Education Series). American Institute of Aeronautics and Astronautics, Jan. 2009.

[24] P. Bartholomew, G. Deskos, R. A. Frantz, F. N. Schuch, E. Lamballais, and S. Laizet, "Xcompact3d: An open-source framework for solving turbulence problems on a cartesian mesh," *SoftwareX*, vol. 12, pp. 100–550, 2020.

[25] S. Laizet and E. Lamballais, "High-order compact schemes for incompressible flows: A simple and efficient method with quasi-spectral accuracy," *J. Comput. Phys.*, vol. 228, no. 16, pp. 5989–6015, 2009.

[26] P. Sagaut, *Large Eddy Simulation for Incompressible Flows: An Introduction*. Berlin, DE: Springer Science & Business Media, Mar. 2006.

[27] O. A. Mahfoze and S. Laizet, "Non-explicit large eddy simulations of turbulent channel flows from Reτ=180 up to Reτ=5,200," *Comput. Fluids*, vol. 228, p. 105 019, May 2021.

[28] J. Manwell, J. McGowan, and A. Rogers, *Wind Energy Explained*. Chichester, UK: John Wiley & Sons, Ltd, Apr. 19, 2002.